Dynamic mechanism of neural circuit refinement in neonatal cortex

中沢　信吾

博士（理学）

総合研究大学院大学
生命科学研究科
遺伝学専攻

平成３０（２０１８）年度

Dynamic mechanism of neural circuit refinement in neonatal cortex

Nakazawa, Shingo

Doctor of Philosophy

Department of Genetics

School of Life Science

SOKENDAI (The Graduate University for Advanced Studies)

Division of Neurogenetics

Department of Developmental Genetics

National Institute of Genetics

2018

ABSTARCT

The brain function is mediated by complex and highly ordered neural circuits. Proper neuronal circuit wiring relies on precise dendritic projection, which is established through activity-dependent refinement during early postnatal development. Here I revealed a dynamic mechanism of dendritic refinement in the mammalian brain by conducting long-term imaging of the neonatal mouse barrel cortex, where layer 4 (L4) spiny stellate (SS) neurons extend basal dendrites (BDs) predominantly toward thalamocortical axons (TCAs) corresponding to single whiskers. By retrospective analysis, I identified prospective barrel-edge SS neurons in early neonates, which had an apical dendrite and primitive BDs. These neurons underwent gradual apical dendrite retraction and continuous BD tree turnover in all directions. Meanwhile, some, but not all, BD trees oriented toward appropriate TCAs became winners, exhibiting longevity and extensive elaboration. When the spatial bias of TCA inputs to SS neurons was absent, BD tree turnover was suppressed, and most BD trees became stable and elaborated mildly. Thus, barrel-edge SS neurons could establish the characteristic BD projection pattern through differential dynamics of dendritic trees induced by spatially biased inputs.

INTRODUCTION

A central question in neuroscience is how cortical circuits are established during postnatal development, wherein initial primitive circuits are refined by periphery-derived neural activity (Goodman and Shatz, 1993; Katz and Shatz, 1996; Sur and Rubenstein, 2005). Dendritic projection patterns of neurons define types of information each neuron receives and processes; thus, it is critical to understand how specific dendritic projection patterns are established during development (Emoto, 2011; Wong and Ghosh, 2002). While some molecules involved in dendritic refinement, in which cortical neurons extend their dendrites toward appropriate presynaptic axons, have been identified (Emoto, 2011; Whitford et al., 2002; Wong and Ghosh, 2002; Wu et al., 2011), how cortical neurons dynamically refine their dendrites and how neural activity regulates these dynamics have remained largely unexplored.

To analyze dendritic refinement of cortical neurons, we have used layer 4 (L4) spiny stellate (SS) neurons in the mouse primary somatosensory cortex (barrel cortex) as a model (Datwani et al., 2002; Iwasato et al., 2000; Iwasato et al., 1997; Iwasato et al., 2008). This area contains “barrels”, which are morphological and functional modules arranged to correspond with facial whiskers (Woolsey and Van der Loos, 1970) (Figure 1a). SS neurons located around the barrel edge (edge-SS or eSS neurons) extend

their basal dendrites (BDs) asymmetrically toward the barrel center, where termini of thalamocortical axons (TCAs) transmitting information from a single whisker form a cluster (Fox, 2008; Woolsey et al., 1975). These characteristic barrel morphologies are formed during the first postnatal week in a periphery-derived input-dependent manner (Harris and Woolsey, 1981; Li et al., 2013; Narboux-Nême et al., 2012), making them a key model of the developmental refinement of cortical circuits. In particular, BD refinement of eSS neurons is an excellent model because in the mouse barrel cortex, an eSS neuron has appropriate presynaptic TCAs only at the side of the barrel center. Therefore, it is possible to quantitatively analyze dendritic projection specificity as BD orientation bias toward the barrel center.

Two-photon microscopy has been widely applied for *in vivo* imaging of structural plasticity in adult neuronal circuits, such as spine formation/elimination associated with learning and memory (Holtmaat and Svoboda, 2009; Yang et al., 2009). For studies of structural plasticity in the developing mammalian brain, two-photon *in vivo* imaging has been used to monitor morphological dynamics of dendritic spines and filopodia of cortical pyramidal neurons (Lendvai et al., 2000; Zuo et al., 2005), climbing fiber axons in the cerebellum (Carrillo et al., 2013), thalamocortical and Cajal-Retzius axons in cortical layer 1 (Portera-Cailliau et al., 2005), and so on. In contrast, technical

difficulties have hindered the use of *in vivo* time-lapse imaging in studies on the dynamics of dendritic development in mammals, which occurs during early postnatal development. Major difficulties include (1) sparse yet intense *in vivo* labeling of neurons, which is necessary for visualization of detailed dendritic morphology, (2) *in vivo* labeling of specific axons that are presynaptic to dendrites of an identified neuron, and (3) use and maintenance of fragile newborn mice during *in vivo* imaging sessions. For these reasons, instead of *in vivo* imaging, acute or chronic slice culture has been predominantly used for two-photon or confocal time-lapse imaging of dendritic development (e.g., dendritic arborization) in the mammalian cortex (Portera-Cailliau et al., 2003), hippocampus (Lohmann et al., 2005; Wayman et al., 2006) and cerebellum (Fujishima et al., 2012). Alternatively, transparent vertebrates such as Xenopus tadpoles (Haas et al., 2006; Sin et al., 2002) and zebrafish larvae (Niell et al., 2004), have been used for *in vivo* time-lapse imaging of dendritic development in the brain and/or retina.

As the first step toward *in vivo* imaging of dendritic refinement in the mammalian brain, our laboratory recently developed two methods: (1) the “Supernova” system, which allows sparse and bright *in vivo* labeling of cortical L4 neurons when used in combination with *in utero* electroporation-based gene transfer (Luo et al., 2016; Mizuno et al., 2014), and (2) TCA-GFP transgenic (Tg) mice, which allows *in vivo*

labeling of TCAs (Mizuno et al., 2014). These innovations have allowed us to conduct short-term (18-h) *in vivo* imaging of SS neuron BDs starting at postnatal day 5 (P5) (Mizuno et al., 2014). This study provided the first *in vivo* observation of dendritic dynamics in the neonatal mammalian brain, in which small-scale dynamics (i.e., elongation/retraction of dendritic branches) were analyzed. However, this study is insufficient, because dendritic refinement is already nearly completed at P5 (See Mizuno et al., 2014). Therefore, to fully understand dynamic mechanisms of BD refinement of SS neurons, long-term (over days) imaging starting at earlier neonatal stages was awaited.

In the current study, I have succeeded in *in vivo* visualization of SS neuron dendrites in mouse pups as early as P3, developing a system by which neonatal mice grow up with adequate maternal care during intervals of imaging sessions over days. Based on these preparations, long-term (3-d-long) imaging of the SS neuron dendrites was achieved and large-scale dendritic dynamics (e.g., emergence/elimination of "dendritic trees") was analyzed. The analysis revealed only a fraction of inner BD trees become "winners", exhibiting high stability and extensive elaboration. Also, I revealed the role of spatial patterns of periphery-derived inputs in the selection dynamics of BD refinement.

In addition, it is important that my long-term imaging of the same neurons over time allowed for “retrospective” identification of prospective SS neurons during early neonatal stages, such as P3. In these stages, most SS neurons show morphological features similar to another type of L4 excitatory neurons, star pyramid (SP) (Callaway and Borrell, 2011). Time-lapse imaging enabled characterization of features of prospective SS neurons at early neonatal stages by using information obtained at later developmental stages (e.g., P6). The retrospective analysis also revealed the presence of two phases in eSS neuron BD refinement during neonatal stages. Thus, the novel *in vivo* imaging system contributes to the understanding of developmental mechanisms of cortical maturation in neonates.

RESULTS

Time-lapse imaging of the same L4 neurons in neonates over 3 days

In L4 of the developing mouse barrel cortex, whisker-specific TCA clusters emerge in the barrel center around P3 (Mizuno et al., 2014), and eSS neurons acquire their characteristic BDs, which are asymmetrically extended within single barrels, primarily by P6 (Espinosa et al., 2009; Mizuno et al., 2014). Therefore, in the present study, to characterize the detailed time course of L4 SS neuron BD refinement, I sought to

perform long-term *in vivo* time-lapse imaging starting at P3 or earlier and ending at P6 (Figure 1b). To visualize the detailed dendritic morphology of individual L4 neurons, L4 neurons were sparsely labeled with RFP using our *in utero* electroporation-based Supernova method (Luo et al., 2016; Mizuno et al., 2014). To visualize the barrel map *in vivo*, TCA-GFP Tg mice expressing EGFP in TCAs (Mizuno et al., 2014) were used (Figures 1c and 1d).

To achieve long-term neonatal imaging over 3 d, it is necessary for pups to have maternal care between imaging sessions. Maternal care is important not only to give pups sufficient nutrition but also to supply them with natural whisker inputs (Akhmetshina et al., 2016) and reduce separation stress that could affect brain development (Krugers and Joels, 2014). However, in initial trials most pups (63%; 5/8 pups) were neglected, killed, and/or injured by mothers within a day after surgery. To solve this problem, I first designed an extremely small titanium bar to help minimize discomfort of mothers during breast-feeding (Figure 1e). Second, I selected foster mothers that showed good results in nursing neonatal mice that had a cranial window/titanium bar. These improvements increased the probability of pups that underwent surgery at P3 (90%; 19/21 pups) or P2 (73%; 8/11 pups) were nursed normally until P6, at which time, the observation was terminated (Figures 1b and 1f).

126 Imaging of L4 neurons was performed repeatedly every 8 h from late P3 ($P3_L$;
127 around 8 PM) to late P5 ($P5_L$) and at late P6 ($P6_L$) (Figures 1b, 1g–1l). In a few cases,
128 imaging was started at late P2 ($P2_L$). Because L4 neurons were sparsely labeled and the
129 relative positions of neurons were roughly conserved, it was easy to identify the same
130 neurons in images taken at different time points (imaging sessions) (Figures 1g and 1j).
131 All neurons (70 neurons from 5 mice) observed at $P3_L$were present at $P6_L$, indicating
132 that there was no cell death during imaging sessions.
133 Time-lapse-imaged (TL) pups significantly increased in body weight from $P3_L$
134 to $P6_L$, as did control pups, and there was no significant difference between TL and
135 control pups even at $P6_L$ (Figure 1m). The barrel field size of $P6_L$ TL pups was larger
136 than that of $P3_L$ controls and similar to that of $P6_L$ controls (Figure 1n), in which
137 cortical tangential sections prepared from TL pups immediately after the $P6_L$ imaging or
138 sections prepared from normal pups at $P3_L$ and $P6_L$ were used. The total BD length and
139 BD tip number of L4 neurons in TL pups increased 3.0-fold and 2.7-fold, respectively,
140 between $P3_L$ and $P6_L$ (Figures 1o and 1q), and both were similar between TL and
141 control pups at $P6_L$ (Figures 1p and 1r). The control analyses were done by *in vivo*
142 imaging of non-TL pups (control), to which a cranial window/titanium bar was attached
143 at P6, and TL pups at $P6_L$. Taken together, these results demonstrate that long-term

imaging over 3–4 d starting at P3 or P2 causes no obvious abnormalities in brain development through $P6_L$.

Two types of L4 neurons distinguished by apical dendrite dynamics

When I compared dendritic morphologies of the same L4 neurons at $P3_L$ and $P6_L$, a striking difference was observed in apical dendrite (AD) (Figure 2a). Most (97%, 36/37) L4 neurons had AD (29.03 to 228.29 μm-long) at $P3_L$, and majority of them lost their AD during later development; at $P6_L$, 54% (20/37) had no AD. Analysis of daily changes in AD length by comparing images of the same L4 neurons taken at $P3_L$, $P4_L$, $P5_L$, and $P6_L$ (also at $P2_L$ in some cases) allowed us to classify individual L4 neurons into two groups (Groups 1 and 2). Neurons which shortened AD during imaging sessions were classified as Group 1 (Figure 2b and Supplementary Figure 1, red lines). In some neurons of Group 1, AD was extended prior to initiation of retraction. One neuron had no AD at $P3_L$ (Supplementary Figure 1), which was also classified as Group 1. On the other hand, neurons that continuously extended AD throughout imaging sessions were classified as Group 2 (Figure 2b and Supplementary Figure 1, blue lines). Based on this criterion, neurons shown in Figures 1h–1i and Figures 1k–1l were classified as Group 1 and Group 2 neurons, respectively. Figures 2c and 2d also show

representative Group 1 and Group 2 neurons, respectively. Among fifty-one L4 neurons analyzed, 76% (39 neurons) and 24% (12 neurons) were categorized as Group 1 and Group 2 neurons, respectively (Table 1).

Morphological aspects of BDs were compared between Group 1 and Group 2 neurons. Increases in the total BD length were not different between the two groups (approximately 3-fold increase in both groups) (Figure 2e). BD orientation bias toward the barrel center of these neurons was analyzed using an orientation bias index (OBI) (See Methods for details).Only the neurons located at the barrel edge were selected for the analysis (Figure 2i and Table 1). I found that at $P6_L$, the OBI of Group 1 neurons was quite high (Figure 2j), indicating that their BDs showed strong orientation bias toward the barrel side, while the OBI of Group 2 neurons was close to 0.5 (Figure 2j), indicating their BDs did not show orientation bias.

In the adult mouse barrel cortex, the majority (65–80%) of L4 neurons are SS neurons with no AD and multiple BDs projecting specifically within a single barrel. The other 20–35% are SP neurons with an AD and multiple BDs showing no orientation bias (Fox, 2008; Lübke and Feldmeyer, 2007; Staiger et al., 2004). In my observation, 76% of L4 neurons were Group 1 and 24% were Group 2. Group 1 neurons possessed no (or short) AD and their BDs exhibited strong orientation bias at $P6_L$, while Group 2 neurons

possessed a long AD and their BDs exhibited no orientation bias. These characteristics of Group 1 and Group 2 neurons were consistent with those of SS and SP neurons, respectively. Therefore, hereafter, Group 1 neurons are referred to as SS neurons and Group 2 neurons as SP neurons, although the possibility cannot be excluded that Group 2 may contain a few SS neurons whose maturation was slower than others.

A recent histological study primarily using the ferret visual cortex demonstrated that virtually all L4 excitatory neurons in early postnatal stages have pyramidal shapes with a long AD and primitive BDs (Callaway and Borrell, 2011). This was confirmed in the current study in the mouse barrel cortex. I also found that prospective SS neurons that exhibit a pyramidal shape lose their AD during development, providing direct evidence for developmental sculpting of SS neuron AD, as proposed by Callaway and Borrell. In addition, I report three new findings. First, the AD was lost from SS neurons by gradual retraction (Figures 2b, 2c). Second, the initiation timing and velocity of AD retraction varied among neurons even in the same animals (Supplementary Figure 1). Third, once ADs started to retract, they did not extend again at least in my observation (Supplementary Figure 1).

Retrospective characterization of prospective eSS neurons

198 Since SS neurons initially had an AD similar to that of SP neurons, it is possible that
199 initiation of AD retraction in SS neurons may precede and/or trigger morphological
200 differentiation. This possibility was examined by the “retrospective” analysis.
201 To elucidate whether SS and SP neurons exhibit morphological differences in
202 early neonatal stages, it is useful to compare the BD orientation bias of SS and SP
203 neurons at $P3_L$. However, at this age, the TCA-GFP signal was too weak to clearly
204 visualize the barrel boundary *in vivo*. In addition, relative positions of SS neurons could
205 shift slightly between $P3_L$ and $P6_L$ due to brain enlargement (Figure 1n) and possibly
206 from SS neuron tangential migration. These issues hindered determination of the precise
207 barrel boundary at $P3_L$. Therefore, the simple version of OBI, which divides BD
208 segment length in the barrel-center half (inside) by total BD length (See Methods for
209 details), was adopted in the current study. The relative positions of individual L4
210 neurons were roughly conserved between $P3_L$ and $P6_L$ (e.g., Figures 1g and 1j),
211 therefore I assumed that the barrel-center direction from each L4 neuron was also
212 conserved. Approximate barrel-center direction was determined by barrel map
213 visualized at later developmental stages (e.g., $P6_L$). In this analysis, only neurons
214 located at the barrel edge at $P6_L$ (eSS and barrel-edge SP (eSP) neurons) were included.
215 Intriguingly, the OBI of eSP neurons was close to 0.5, and that of eSS neurons was

significantly larger than that of eSP neuron BDs at $P3_L$ (Figure 2g), suggesting that eSS neurons already had BD orientation bias toward the barrel center as early as P3, when TCA termini start to form clusters in the barrel center (See Figure 3D of Mizuno et al., 2014). Then, OBI quantification was repeated using only eSS neurons that had an intact AD at $P3_L$ (See Methods for details). Again, the OBI of these neurons was significantly larger than that of eSP neurons at $P3_L$ (Figure 2h), although AD lengths were similar between these two groups of neurons at this age (eSS neurons with intact AD, 165.0 ± 7.6 μm; eSP, 166.0 ± 12.2 μm). Thus, SS neurons have the morphological feature distinct from SP neurons, even before initiation of AD retraction. In other words, initiation of AD retraction is not the cause or trigger of SS neuron differentiation.

I then examined which aspects of BD morphology contribute to the initial orientation bias of prospective eSS neurons at P3 through detailed analysis of BD morphologies (Figure 3). In the current study, my analyses were focused mostly on “BD trees” rather than BD branches, because it appeared to be more informative for the reason described later. BD tree indicate the primary dendrite and its branches (e.g., Figure 3e, scheme of $P6_L$ neuron, orange colored segments compose one tree). BD trees were categorized into 2 groups: “inner trees” with origins located in the barrel center-side half (inside) and “outer trees” with origins on the opposite side (outside). At $P3_L$,

234 the number of inner trees of eSS neurons was significantly larger than that of outer trees
235 (Figure 3c, $P3_L$). On the other hand, lengths and tip numbers of individual trees were
236 similar inside and outside in both eSS (Figures 3e and 3f, $P3_L$). These results suggest
237 that BD orientation bias of eSS neurons at $P3_L$ is not accomplished by differential
238 elaboration of individual inner and outer trees, but rather by the difference in the
239 numbers of trees inside and outside the barrel.
240

241 **Two phases in eSS neuron BD refinement in neonates**

242 Although prospective eSS neurons already showed some BD orientation bias at $P3_L$, BD
243 morphology was still primitive at this stage, precluding more extensive directionality.
244 However, BDs elaborated dramatically between $P3_L$ and $P6_L$ (Figures 2e and 3a) and
245 this was accompanied by a significant increase in OBI (Figure 3b). I next examined
246 which aspects of BD morphological changes influenced the OBI increment of eSS
247 neurons between $P3_L$ and $P6_L$. The ratio of inner tree numbers to total ones did not
248 increase between P3 and P6 (Figure 3d). In contrast, the length of individual inner trees
249 was significantly larger at $P6_L$ than at $P3_L$ (Figure 3e, inside). In addition, individual
250 inner trees had more tips at $P6_L$ than at $P3_L$ (Figure 3f, inside). On the other hand, the
251 lengths and tip numbers of individual outer trees were similar between $P3_L$ and $P6_L$

(Figures 3e and 3f, outside). These results suggest that OBI enhancement of eSS neurons between $P3_L$ and $P6_L$ primarily relies on inner BD tree-selective elaboration rather than outer BD tree-selective retraction or an increased ratio of inner to total BD tree.

These results also suggest that eSS neurons acquire BD orientation bias at least in two phases during the first postnatal week (Figure 3g). By P3 (Phase I), eSS neurons produced more inner BD trees than outer BD trees, although both inner and outer BD trees are morphologically simple at this stage. After P3 (Phase II), the ratio of inner/outer trees from eSS neurons does not change, but inner BD trees become more elaborate.

Differential turnover and elaboration of BD trees in eSS neurons

Next question is how eSS neuron BDs are refined during Phase II. In the initial trial, "dendritic branch" dynamics (e.g., elongation/retraction) was analyzed as shown in our previous work(Mizuno et al., 2014). However, this approach was not appropriate for the current work. Morphological changes of BDs in 3 days were enormous (e.g., Figure 1g), and therefore dendritic branch analyses were too complicated to yield a meaningful outcome. After a trial-and-error, I found that focusing on "dendritic trees" rather than

270 “dendritic branches” was more informative in understanding how the eSS neurons
271 acquire their characteristic BD orientation bias.

272 The spatiotemporal dynamics of individual trees was investigated between $P3_L$
273 and $P5_L$ over 8-h intervals (Figure 4). Strikingly, BD trees emerged and disappeared
274 extensively throughout the imaging period (Figures 4a–4c). Emergence of new trees
275 was not restricted to inside but observed both inside and outside (Figure 4d). Similarly,
276 tree elimination was not restricted to outside, but observed both outside and inside
277 (Figure 4e). Of outer trees newly emerged between $P3_L$ and $P5_M$ (around P5 noon), 82%
278 (18/22) disappeared by the next imaging session (one time-frame), and only a small
279 portion of outer trees survived longer than one imaging interval (Figures 4f). In contrast,
280 only 31% (5/16) of newly emerged inner trees disappeared within one time-frame, and a
281 substantial portion survived longer (Figures 4g). Thus, the survival efficiency was
282 significantly higher for inner trees than outer trees (Figure 4h).

283 Then the relationship between survival time and length of individual trees was
284 examined by focusing on trees newly emerged during imaging sessions. These trees
285 were categorized into 4 groups: “surviving inside,” “surviving outside,” “eliminated
286 inside,” and “eliminated outside.” Surviving trees were those present at $P5_L$ (the final
287 imaging session), and eliminated trees were those that disappeared during imaging

sessions. The lengths of surviving inner trees increased in proportion to survival time-frames (Figure 4i), while outer trees remained short. Although a few outer trees survived for a long time and elaborated, most of them extended their arbors toward the inside of the barrel (e.g., Figure 4j). These results suggest that long survival is preferentially conferred to some (but not all) trees that extend toward TCAs and that only these trees (mostly inner) become "winners," which subsequently elaborate over time. Importantly, the winner trees were not necessarily early-emerging. In other words, trees that were born later also had the chance to survive and elaborate (e.g., Figure 4k).

Taken together, I found that eSS neuron BD trees in the neonatal barrel cortex exhibit extensive turnover in all directions. During this dendritic tree turnover, a fraction of inner trees survived, and these surviving inner trees were extensively elaborated, which contributed to reinforcement of BD orientation bias between P3 and P6.

BD tree dynamics in eSP neurons

I next analyzed the BD tree characteristics of eSP neurons. The numbers of inner and outer trees were similar both at $P3_L$ and $P6_L$ (Supplementary Figure 2a). The lengths and numbers of tips of individual BD trees were also similar between inside and outside both at $P3_L$ and $P6_L$ (Supplementary Figures 2b and 2c). These results indicate that BD

306 tree outgrowth of eSP neurons is not influenced by the existence of TCAs. The BD tree
307 turnover of eSP neurons was also measured. The results show that eSP neurons
308 exhibited BD tree turnover as eSS neurons did (Supplementary Figures 2d and 2e),
309 although the samples size was limited. Note that, in my classification, if an SS neuron
310 starts to retract its apical dendrite after P6, this neuron is categorized as SP neuron.
311 Therefore, we cannot exclude the possibility that a few neurons which were classified as
312 SP neurons are SS neurons whose development was slow.
313

314 **BD tree dynamics in barrel-center SS (cSS) neurons**

315 Each eSS neuron receives appropriate TCA inputs using mostly inner BD trees. To
316 understand whether this spatial bias of TCA inputs is involved in the differential
317 dynamics of BD trees described above, dendritic dynamics of SS neurons located in the
318 barrel center (cSS neurons) was examined (Figure 5a). The cSS neurons could receive
319 TCA inputs by all BD trees, and therefore have little or no spatial bias in TCA inputs.
320 Several parameters of BD (and BD tree) growth were similar between eSS and
321 cSS neurons, in which the data of inner and outer BD trees from eSS neurons were
322 pooled (Supplementary Figures 3e–h). Intriguingly, however, the variance in length of
323 individual BD trees of cSS neurons was smaller than that of eSS neurons at $P6_L$

(Supplementary Figure 3h). To visualize the difference more clearly, the histograms (Figures 5c and 5d) and cumulative curves (Supplementary Figure 3i and 3j) were constructed. In these analyses, inner and outer trees of eSS neurons were distinguished. In eSS neurons at $P3_L$, lengths of most inner and outer BD trees were close to the mean value (inside, 64.1 μm; outside, 67.1 μm) (Figure 5c and Supplementary Figure 3i), while at P6, the ratio of trees which have lengths close to the mean (inside, 170.1 μm; outside, 96.0 μm) was decreased both inside and outside (Figure 5d and Supplementary Figure 3j). Instead, short trees were drastically increased both inside and outside, and long trees were increased only inside (Figure 5d and Supplementary Figure 3j). On the other hand, most BD trees of cSS neurons had lengths close to mean values ($P3_L$, 60.8 μm; $P6_L$, 152.7 μm), and shorter and longer trees were rare at both ages (Figures 5c and 5d and Supplementary Figures 3i and 3j). It is important that the growth characteristics of cSS neuron BD trees differed from those of eSS neuron inner BD trees, although both could receive TCA inputs, suggesting the possible significance of spatial bias of TCA inputs, not just the presence of TCA inputs, in dendritic refinement dynamics.

Analyses of BD tree turnover also revealed intriguing differences between eSS and cSS neurons. The BD trees of cSS neurons tended to live longer than those of eSS neurons (Figure 5e). The numbers of eliminated trees per neuron were significantly

smaller in cSS neurons than eSS neurons between $P3_L$ and $P5_L$ (Figure 5h). cSS neurons tended to have fewer newly formed BD trees than eSS neurons, although the difference was not significant (Figure 5g). These results demonstrate that BD trees from cSS neurons exhibit little turnover and most live long and grow mildly, suggesting that dynamics of BD trees can be affected by the spatial distribution of TCA inputs.

BD tree dynamics in pups with early infraorbital nerve cut

Infraorbital nerve (ION) cut is a commonly used method to block the neural activity in the mouse somatosensory system (Supplementary Figure 3a). When ION is severed in early neonates such as at P0, barrel map formation is completely impaired (Erzurumlu and Gaspar, 2012; Waite and Cragg, 1982) as shown in Supplementary Figure 3b. On the other hand, the ratio of AD-possessing neurons was not different from that of normal mice at P16 (Supplementary Figure 3c).

To understand the effects of early ION-cut on BD and BD tree growth, the ION was severed at P0 mice, and time-lapse imaging of SS neurons was performed in these pups (Early-ION-cut mice) (Figure 5b and Supplementary Figure 3d). At $P3_L$, BD (and BD tree) morphology of SS neurons in ION-cut mice (iSS neurons) was similar to that of eSS and cSS neurons (Figure 5c and Supplementary Figures 3e–i). At $P6_L$, however,

the variance in length of individual BD trees from iSS neurons was similar to that from cSS neurons but significantly smaller than that from eSS neurons (Supplementary Figure 3h). In iSS neurons, most BD trees had lengths close to mean values (137.8 μm), while substantially shorter and longer trees were rare (Figure 5d and Supplementary Figure 3j). Analyses of BD tree turnover also showed that most trees of iSS neurons lived as long as those of cSS neurons (Figure 5f). The numbers of newly formed and eliminated trees per neuron between $P3_L$ and $P5_L$ were also similar between iSS neurons and cSS neurons but significantly smaller than those in eSS neurons (Figures 5g and 5h). These results suggest that BD tree dynamics of iSS neurons are similar to cSS neurons.

Early ION cut alters spatial patterns of spontaneous activity

We recently report unique features of spontaneous activity in neonatal barrel cortex L4, which shows a “patchwork”-type pattern corresponding to the barrel map. This patchwork activity is delivered to L4 via TCAs. We conducted ION cut at P4 or P5 (Late-ION-cut) and found that the patchwork activity was not affected (Mizuno et al., 2018). Importantly, Late ION cut did not affect the gross formation of barrel map. On the other hand, when IONs were cut at P0 (Early-ION-cut), barrel map formation was

impaired (Supplementary Figure 3a and 3b). I examined if Early ION cut could affect the patchwork activity by using TCA-GCaMP Tg mice (Mizuno et al., 2018) in cooperation with Dr. Mizuno. Calcium signals of TCA terminals in large-barrel field between control and Early-ION-cut mice (Figure 6) were compared. Spontaneous activity occurred in both groups, but their features were different between the groups. In control mice, the boundaries of activated zones were invariable and corresponded to the boundaries of individual barrels (Figures 6a and 6b). In contrast, they were variable in Early-ION-cut mice (Figures 6f and 6g). In addition, the mean area of single activated zones was more than 4.5 times larger than that of control mice (Figure 6k). To further examine the effects of early ION cut on spontaneous activities, the regions of interest (ROIs) were placed on the large-barrel field of the somatosensory cortex of control and ION-cut mice (Figures 6c and 6h). Color-coded correlation matrices constructed from the fluorescence changes (Figures 6d and 6i) clearly showed that there are high-synchrony zones, which corresponded to barrels, in control mice (Figure 6e). In contrast, such zones were not detected in the Early-ION-cut mice (Figure 6j). The frequencies of activated events were not much different between Early-ION-cut and control mice (Figures 6d, 6i and 6l), although it should be noted that precise comparison of frequencies is difficult because spatial patters and sizes of activated zones were very

different between the two groups. These results suggest that the Early-ION-cut mouse barrel cortex still receives spontaneous activity via TCAs, but this activity no longer exhibits the patchwork pattern.

In contrast, Late ION cut does not affect the spatial pattern of spontaneous activity (Mizuno et al., 2018). These results indicate that whisker-derived inputs in early neonatal stages such as P0, but not in later stages such as P4 or P5, are essential to patchwork patterning of spontaneous activity.

In normal mice, SS neurons located at the barrel edge (i.e., eSS neurons) receive spatially biased TCA inputs only from one direction (i.e., toward the barrel center). On the contrary, like cSS neurons in normal mice, SS neurons of ION-cut mice (i.e., iSS neurons) should not have any specific direction for proper TCA inputs. It is likely that this disruption of polarized TCA-inputs results in altered dynamics of iSS neurons.

DISCUSSION

To my knowledge, the present study is the first to report long-term (days) *in vivo* imaging analysis of dendritic dynamics in developing mammals. Herein, I have successfully accomplished *in vivo* imaging of the mouse barrel cortex starting at P3 and ending at P6. The present result reveals dynamics of SS neuron BD trees associated with circuit refinement in the neonatal barrel cortex, as well as possible involvement of spatial patterns of periphery-derived inputs in these dendritic tree dynamics as summarized in Figure 7 (see legends). Furthermore, long-term imaging of the same neurons enabled to retrospectively identify prospective SS neurons and characterize their features in early neonatal stages (e.g., P3) when SS neurons are indistinguishable from SP neurons by conventional methods.

Dynamic mechanism of dendritic refinement in the neonatal barrel cortex

ION cutting blocks sensory inputs from whiskers but not spontaneous activity, which is most likely derived from the trigeminal ganglion or further downstream (Lo and Erzurumlu, 2016; Minnery and Simons, 2002; Mizuno et al., 2018; Shoykhet et al., 2003). The result showed that the spatial pattern of the spontaneous activity was disrupted by ION-cut at P0 (Figure 6, Supplementary Figure 3a and 3b). In ION-cut

427 mouse cortex, the ratio of AD-possessing L4 neurons did not decrease (Supplementary
428 Fig. 3c), supporting the notion that L4 neurons receive TCA inputs in ION-cut mice,
429 because in the absence of TCA inputs most L4 neurons fail to eliminate the AD
430 (Callaway and Borrell, 2011; Li et al., 2013). In the normal mouse cortex, each eSS
431 neuron receives TCA inputs (both sensory-evoked and spontaneous) from specific BD
432 trees, which are oriented toward the barrel center. In contrast, in the cortex of ION-cut
433 mice, SS neurons (i.e., iSS neurons) should not have any dominant BD trees to receive
434 TCA inputs because spontaneous activity no longer exhibits a patchwork pattern (Figure
435 6). It is intriguing that BD tree dynamics of iSS neurons are similar to those of cSS
436 neurons (Figures 5g and 5h). In both cases, TCA inputs should not have specific spatial
437 bias to SS neurons.

438 It appears that spatially biased TCA inputs to SS neurons facilitate cell-wide
439 BD tree turnover, because turnover rate is higher in eSS neurons than in cSS and iSS
440 neurons. Another scenario is that biased distributions of physical structures of TCA
441 clusters and/or unidentified molecules derived from TCAs could induce high levels of
442 BD dynamics in eSS neurons. Although these possibilities cannot be excluded, previous
443 studies oppose them. For example, mice in which the gene encoding the NMDA
444 receptor NR1 subunit is knocked out in single SS neurons showed normal TCA clusters

445 but impaired BD refinement (Mizuno et al., 2014). The RIM1/RIM2 double knockout
446 mice, which lack thalamocortical synaptic transmission, also show overtly normal TCA
447 clustering but impaired BD refinement (Narboux-Nême et al., 2012). These results
448 clearly demonstrate that the presence of physical TCA clusters are not sufficient and
449 synaptic inputs from TCAs to SS neurons are necessary for BD refinement.

450 Previous *in vivo* imaging studies using the tectum of Xenopus tadpole or
451 zebrafish larvae suggested that dendritic branches are stabilized and elaborated by
452 forming synapses with axons, and that glutamate receptor (NMDA and AMPA
453 receptor)-mediated synaptic transmission is important for this stabilization process
454 (Haas et al., 2006; Niell et al., 2004; Sin et al., 2002). The previous study of short-term
455 (hours) *in vivo* imaging of mouse barrel cortex eSS neurons in our laboratory also
456 revealed an important role for NMDA receptors in stabilization of BD branches
457 (Mizuno et al., 2014). It is likely that postsynaptic signaling induced by NMDA and/or
458 AMPA receptors stabilizes those BD branches that make synaptic contact with
459 appropriate TCAs, which in turn stabilizes the tree (and makes it a “winner” in the
460 competition for thalamic inputs).

461 Gene knockout and knockdown approaches have identified many molecules
462 involved in SS neuron BD refinement, including the NMDA receptor, metabotropic

463 glutamate receptor 5, adenylyl cyclase 1, protein kinase A, BTBD3, and Lhx2
464 (Ballester-Rosado et al., 2010; Datwani et al., 2002; Inan et al., 2006; Iwasato et al.,
465 2000; Iwasato et al., 1997; Iwasato et al., 2008; Matsui et al., 2013; Mizuno et al., 2014;
466 Wang et al., 2017). In future, it will be important to examine how each of these
467 molecules is involved in BD refinement dynamics of barrel cortex SS neurons. Our
468 Supernova system, which enables single-cell labeling and labeled cell-specific gene
469 manipulation, could facilitate further understanding of molecular mechanisms operating
470 in individual SS neurons (Luo et al., 2016). It is also important to understand
471 developmental changes of spontaneous activity in individual neurons and populations,
472 using long-term calcium imaging (and simultaneous imaging of dendritic morphology).
473 In the mammalian brain, developmental dendritic refinement is found not only in barrel
474 cortex SS neurons, but also in various types of neurons in other brain areas, such as SS
475 neurons in L4 of the visual cortex (in some animals) (Katz and Shatz, 1996; Kossel et
476 al., 1995), Purkinje cells in the cerebellum (Fujishima et al., 2012; Takeo et al., 2015),
477 and mitral cells in the olfactory bulb (Lin et al., 2000). Long-term *in vivo* imaging will
478 be a powerful method for uncovering dynamic mechanisms of dendritic refinement in
479 these neurons and the cellular and molecular mechanisms regulating these dynamics.
480

Two phases in BD refinement of SS neurons during neonatal stages

As described above, at P3, eSS neurons already have orientation bias, which is ascribed by the difference in number of inner and outer BD trees (Figures 2g and 3c). On the other hand, at P6, the ratio of inner BD trees to the total was similar to that at P3 (Figure 3d), but the complexity of the inner BDs was much higher than that at P3 (Figure 3e and 3f). These results suggest that there are at least two distinct phases in the formation of BD orientation bias in neonates (Figure 3g). Phase I is approximately between P0 and P3. Around P0, L4 neurons radially migrate to their final positions and start to elaborate BDs (Callaway and Borrell, 2011). Then by P3, L4 eSS neurons create nascent orientation bias by forming more BD trees inside than outside. At this stage, both inner and outer BDs are similarly primitive. It is possible that TCAs secrete molecules that produce more BD trees on the side of the barrel center, where TCA termini form a cluster by P3 (Mizuno et al., 2014), although neural activity transmitted through TCAs could also be involved. In contrast, Phase II starts approximately at P3 and ends at P6 or later. In this phase, the ratio of inner to total BD trees does not change. Instead, stability and elaboration are primarily conferred upon a fraction of inner BD trees (Figures 4h and 4i), which results in reinforcement of orientation bias toward the barrel side.

Spiny stellate neurons may have homeostatic mechanisms to maintain BD tree

numbers, because these numbers did not change substantially between P3 and P6 (Figure 3c). If so, rapid elimination of unselected trees could be useful for producing more new trees ("challengers" for inputs). New winner trees continue to emerge from challenger trees predominantly near the barrel center, where TCAs are clustered. By this mechanism, the highly asymmetric pattern of eSS neuron BD projections toward the barrel center could be established.

My detailed analyses of dynamic mechanisms of Phase II provided an important future perspective is to characterize aspects of BD formation in Phase I, which was newly found in the current study.

In the current study, I successfully conducted long-term *in vivo* imaging of cortical neuron dendrites in early neonatal stages. This novel approach revealed a dynamic mechanism of dendritic refinement of barrel cortex SS neurons. In addition, my retrospective analysis based on long-term *in vivo* time-lapse imaging highlights the novel features of L4 neurons in early neonatal stages.

METHODS

Animals

All experiments were performed according to the guidelines for animal experimentation of the National Institute of Genetics (NIG) and were approved by the animal experimentation committee of the NIG. To obtain pups, ICR female mice were mated with male TCA-GFP Tg mice (Mizuno et al., 2014) which were backcrossed from B6 to ICR more than four times or male TCA-GCaMP Tg mice (Mizuno et al., 2018) which were backcrossed from B6 to ICR more than 1 time. The day at which the vaginal plug was detected was designated as embryonic day 0 (E0) and E19 was defined as postnatal day 0 (P0). For histological analysis of infraorbital nerve (ION)-cut mice (Supplementary Figure 3c), timed-pregnant ICR mice were obtained from CLEA Japan. Sex of newborn mice was not determined.

Surgery

In utero electroporation was conducted as described (Mizuno et al., 2007). Briefly, pregnant mice at 14 postcoitus days were anesthetized with an intraperitoneal injection of sodium pentobarbital (50 mg/kg) in saline. Isoflurane was used to control anesthesia level. A midline laparotomy was performed to expose the uterus. DNA solution mixed with trypan blue (< 5%, Sigma) was injected into the right lateral ventricle of embryos via a pulled glass capillary (Drummond), and square electric pulses (40 V; 50 ms) were delivered five times at the rate of one pulse per second by a CUY21SC electroporator (NepaGene). After electroporation, the uterus was repositioned, and the abdominal wall and skin were sutured. After surgery, pregnant mice were kept on a 37°C heater until they recovered from anesthesia.

Infraorbital nerve (ION) cutting (Erzurumlu and Gaspar, 2012; Waite and Cragg, 1982) was performed as follows (Supplementary Figure 3a): Pups at P0 were anesthetized with isoflurane, and a vertical incision was made on the posterior edge of the left whisker pad and the IONs were cut. After the operation, pups were kept on a warm plate and revived, after which they were returned to mothers.

Craniotomy for time-lapse *in vivo* imaging was performed as described (Mizuno et al., 2014) with some critical modifications. For *in vivo* time-lapse imaging of P2 and P3 mice, which are much smaller and more fragile than P5 mice, I newly designed the titanium bar that was very light (~20 mg) and small (7 × 2 × 0.5 mm) (T and I) and used the round cover glass whose diameter is 2.5 mm (Matsunami). In the morning of P2 or P3, mice were anesthetized with isoflurane. Skin covering the right hemisphere was removed using scissors to expose skull followed by applying of Vetbond (3M) to fix the margin and to stop bleeding. Barrel area was detected by TCA-GFP signal and a small piece of bone covering the Supernova-labeled barrel area was removed with a sterilized razor blade, keeping the dura intact. Gelfoam (Pfizer) was used to stop bleeding, as necessity. To keep the brain moist, cortex buffer (Holtmaat et al., 2009) (125 mM NaCl, 5 mM KCl, 10 mM glucose, 10 mM Hepes, 2 mM $CaCl_2$, and 2 mM $MgSO_4$; pH 7.4) was applied during surgery. After that, the window was covered with 1% low melting point agarose (Sigma) in cortex buffer and 2.5 mm diameter round cover glass. The custom-made titanium bar was glued to the skull near the window to attach mouse to two-photon microscope stage (Figure 1e). The dental cement was applied to secure the exposed region. For analgesic and anti-inflammation, carprofen (5 mg/kg, Zoetis) was subcutaneously injected. After recovery, pups were returned to real or foster mothers.

562 Craniotomy for *in vivo* calcium imaging was performed as described (Mizuno
563 et al., 2018). Briefly, P5 or P6 pups were anesthetized by isoflurane and the skull over
564 the barrel field was removed. 1% low melting point agarose in cortex buffer (Holtmaat
565 et al., 2009) was applied to cover the exposed dura and the window was sealed with 3
566 mm diameter round cover glass (Matsunami) that secured with dental cement. A
567 titanium bar (Mizuno et al., 2014) (~30 mg) was attached to the area adjacent to the
568 cranial window. After surgery, pups were kept on a heater for recovery.
569
570 Long-term *in vivo* imaging of L4 in neonatal mice
571 For long-term time-lapse imaging of L4 neurons in the large-barrel field of the primary
572 somatosensory cortex, TCA-GFP (Mizuno et al., 2014) pups, in which L4 neurons were
573 sparsely labeled by *in utero* electroporation-based Supernova-RFP (Luo et al., 2016)
574 [pK036.TRE-flpe-WPRE (10–15 ng/μl) and pK037.CAG-FRT-STOP-FRT-RFP-ires-
575 tTA-WPRE (1,000 ng/μl)], were anesthetized with 0.8%–1.2% isoflurane and fixed to
576 the microscope stage using the titanium bar. Heating pad was used to keep pups warm.
577 Images were acquired using an LSM 7MP two-photon microscope (Zeiss) with a W
578 Plan-Apochromat 20x/1.0 DIC objective lens (Zeiss) and an LSM BiG detector (Zeiss).
579 HighQ-2 laser (Spectra-Physics) at 1,045 nm was used in most experiments. GFP and
580 RFP were simultaneously excited and emitted fluorescence was filtered (500−550 nm
581 for GFP and 575−620 nm for RFP). In an experiment (mouse ID #227, See Table 1),
582 Mai Tai eHP DeepSee titanium-sapphire laser (Spectra-Physics) running at 1,000 nm
583 was used.
584 Images were taken at $P3_L$, $P4_E$, $P4_M$, $P4_L$, $P5_E$, $P5_M$, $P5_L$, and $P6_L$ (mouse ID
585 #231, #239, #269, #270, #356); at $P2_L$, $P3_E$, $P3_M$, $P3_L$, $P4_E$, $P4_M$, $P4_L$, $P5_L$, and $P6_L$

(#260, #315); at $P3_L$, $P4_L$, $P5_L$, and $P6_L$ (#205); at $P3_L$, $P4_E$, $P4_M$, $P4_L$, $P5_L$, and $P6_L$ (#227); at $P2_L$, $P3_E$, $P3_M$, $P3_L$, $P4_E$, $P4_M$, $P4_L$, $P5_E$, $P5_M$ and $P5_L$ (#313); at $P2_L$, $P3_E$, $P4_L$, $P5_L$, and $P6_L$ (#314). PX_E, $PX_{M,}$ and PX_M indicate around 4 am, noon, and 8 pm at postnatal day X (PX) as shown in Figure 1b. Body weight was measured before or after each imaging session. Pups were returned to mothers during the interval between imaging sessions. Low body temperature, bleeding, chemical smell and human smell of pups could result in neglect by mothers. Therefore, pups were kept on a warm heater and with mother's bedding before returning to the mother. It was confirmed that time-lapse imaged pups received proper maternal care and drunk enough breast milk (Figure 1f).

Histological analyses after the end of *in vivo* imaging confirmed that all analyzed neurons of both normal and ION-cut mice were located within the large-barrel field of the primary somatosensory cortex (See also Table 1). Brain samples were prepared immediately after the $P6_L$ imaging session. Mice were decapitated, and brains were fixed with 4% paraformaldehyde (PFA) in 0.1 M PB at 4°C for 1–3 d. For tangential sectioning, right hemispheres were flattened and transferred to 2% PFA/30% sucrose in 0.1 M PB. Flattened cortex was kept at 4°C for 1–2 d and tangential slices (100 μm-thick) were obtained with a ROM-380 freezing microtome (YAMATO). Slices were mounted with Anti-fade Mounting Medium (Longin et al., 1993). Images were acquired by a TCS SP5 confocal microscope (Leica). The layout of the barrel map was identified by TCA-GFP signals.

Barrel field size measurements

Barrel field size (Figure 1n) was measured from confocal images by using Fiji/ImageJ

610 1.51p (Schindelin et al., 2012). The area of the large-barrel area visualized by GFP
611 signal of TCA-GFP mice was measured.
612
613 Quantification of 3-dimentional dendritic morphology
614 Autoaligner 6.0.1 (Bitplane) was used to reduce the noise from respiratory movements.
615 For tracing and quantification, Imaris Filament Tracer 7.0 and 8.3 (Bitplane) were used.
616 Only neurons of which all BD and AD terminals were clearly visible were used for BD
617 and AD analyses, respectively. Dendrite traces were generated semi-automatically and
618 validated manually. Any dendritic processes greater than 5 μm in length was designated
619 as a dendritic segment. Dendritic trees of which origins were in the same position
620 between time-sequential images were considered as the same tree. Apical dendrite (AD)
621 and basal dendrites (BDs) were distinguished by their shape at the initial imaging
622 session. Dendrites that had the same orientation as neighboring neuron ADs were
623 judged as ADs. At early neonatal stages, neurons usually had single long thick AD
624 toward pial surface. Axon was distinguished from BDs by the following features; 1)
625 Axon was thinner than BD. 2) Axon emerged from the bottom of the soma. 3) Axon
626 projected toward deep brain regions. All imaged neurons were categorized either Group
627 1 (SS) or Group 2 (SP) neurons as follows: Group 1 neuron was the neuron that
628 shortened AD during imaging sessions or the neuron which had no AD at $P3_L$ (Figure 2b
629 and Supplementary Figure 1, red lines); Group 2 neuron was the neuron that
630 continuously extended AD throughout imaging sessions (Figure 2b and Supplementary
631 Figure 1, blue lines). SS neurons with intact AD (Figure 2h) was Group 1 neurons
632 whose AD started to retract after $P3_L$.
633

Quantification of BD orientation

Because mice were detached from the two-photon microscope stage after each imaging session, orientations of acquired images were slightly different among imaging sessions. Prior to dendritic orientation analyses, these orientation artifacts among images were adjusted as follows: For each z-stack two-photon image, neuronal coordinates were measured by Fiji/ImageJ as centroids of binary images. The central point of each image was determined by the centroid of neuronal coordinates. The central points of images were laid over and images were rotated around the central point. Angle difference between two images was calculated to minimize the error (determined by the least squares method) between coordinates of same neurons in two images. The orientation artifact was corrected by applying this angle difference to the image (e.g., white rectangles in Figures 1g and 1j).

The layout of the barrel map was identified by TCA-GFP signals of *in vivo* images and/or tangential section images taken at $P6_L$ (and one case at $P5_L$ due to accidental animal death). The barrel edge was determined by the contrasting difference of TCA signal intensities in the area lying between barrel center and septa. Neurons whose cell-body center was located within 12.5 μm from the barrel edge were classified as barrel-edge neurons. Other neurons located within the barrel were classified as barrel-center neurons. The simple version of orientation bias index (OBI), which was used in the current study, was defined as the ratio of BD segment length in the barrel-side half to the total BD length. Inside-Outside boundary, which separates barrel-side half and the other half, was determined as follows. First, a 100 μm-diameter circle that had its center on the cell body was drawn. Second, a line passing through the intersections of the 100 μm-diameter circle and TCA cluster boundary was drawn. Then,

the Inside-Outside boundary which passes through the cell body was drawn parallel to the line. Barrel-side half and the opposite-side half of the boundary were defined as "Inside" and "Outside", respectively. Each BD segment length is the length between two branch points or length between a branch point and the branch tip (or origin of the dendritic tree). An inner BD segment is the segment all or majority of whose length belongs to the barrel-side half.

In vivo calcium imaging

In vivo calcium imaging was performed for the large-barrel field of the primary somatosensory cortex L4 of TCA-GCaMP pups (Mizuno et al., 2018) at P5 or P6 under an unanesthetized condition. In these mice, L4 neurons were sparsely labeled by *in utero* electroporation-based Supernova-nlsRFP [pK031.TRE-Cre (Mizuno et al., 2014) (10 ng/μl) and pK263.CAG-loxP-STOP-loxP-nlsRFP-ires-tTA-WPRE (Mizuno et al., 2018) (1,000 ng/μl)] as markers of the *in vivo* imaged areas. Images were acquired at 1 Hz (512 × 512 pixels) using an LSM 7MP two-photon microscope (Zeiss) with a W Plan-Apochromat 20x/1.0 DIC objective lens (Zeiss) and an LSM BiG detector (Zeiss). Mai Tai eHP DeepSee titanium–sapphire laser at 940 nm was used. Emitted fluorescence was filtered 500−550 nm for GCaMP6s and 575−620 nm for nlsRFP. During imaging, the body temperature of the pup was maintained using a heating pad. When the pup head moved during imaging, these frames were excluded from the analyses.

The boundaries of activated zones (Figures 6a, 6b, 6f, 6g and 6k) were determined as follows. Each image was spatially smoothed with a Gaussian filter (Sigma = 10 px). $\Delta F/F = (F - F_0)/F_0$ was calculated in each pixel at each time. F_0 of

each pixel was obtained by averaging more than 50 images in which calcium transients were obviously absent such as under anesthesia. $\Delta F/F > 100\%$ were considered as activated pixels. With these criteria, boundaries of activated zones were best matched with the barrel edges in control mice. The zones that were less than 2,500 μm^2 were excluded as noise.

The fluorescence intensity traces (Figures 6d and 6i), which were used for raster plots (Figures 6d and 6i) and correlation matrices (Figure 6e and 6j), were generated from sequential 3-minutes images as follows. Forty (5 × 8) regions of interest (ROIs: 20 μm diameter) were positioned on large-barrel field of the somatosensory cortex L4 with 50 μm intervals (Figure 6c and 6h). F of ROI was obtained by averaging intensities of pixels inside the ROI. F_0 of each ROI was obtained by averaging more than 50 images in which calcium transients were obviously absent. For the raster plots, the threshold $\Delta F/F > 50\%$ was used, because with this condition calcium transients in the control mice were most accurately detected. With the threshold $\Delta F/F > 100\%$, although the barrel boundaries in control mice were most sharply visible, some apparent calcium transients (typical patchwork-activity (Mizuno et al., 2018)) were failed to be detected (high false-negative ratio). Correlation matrices were sorted by principal component analysis with a few exceptions (See Figure 6e legend). Calcium imaging data were analyzed by custom-written scripts in Python and ImageJ/Fiji.

Histological analyses after the *in vivo* calcium imaging confirmed that all analyzed neurons of both normal and ION-cut mice were located within the large-barrel field of the primary somatosensory cortex. Tangential sections were permeabilized and blocked in 0.2% Triton X-100/5% normal goat serum (Sigma) in 0.1 M PB. Rabbit anti-VGluT2 (1:1000; Synaptic systems #135403) and Alexa 488-conjugated goat anti-rabbit

706 IgG (1:1000; Invitrogen #A11034) antibodies were used. Although, in the ION-cut
707 mouse cortex, barrel map is impaired, still identification of the large-barrel field was
708 possible.
709
710 Measurement of ratio of neurons with apical dendrite
711 L4 neurons were labeled by *in utero* electroporation-based Supernova (Luo et al., 2016)
712 [pK036.TRE-flpe-WPRE (10–15 ng/μl) and pK037.CAG-FRT-STOP-FRT-RFP-ires-
713 tTA-WPRE (1,000 ng/μl)]. P16 mice in which IONs were cut at P0 (or uncut as control)
714 were perfused by saline and 4% PFA in 0.1 M PB before decapitated. Brains were fixed
715 with 4% PFA in 0.1 M PB at 4°C for 3 d. Then, brains were transferred to 30% sucrose
716 in 0.1 M PB and kept at 4°C for 1–2 d. Coronal slices (100 μm-thick for most
717 experiments and 50 μm-thick for cytochrome oxidase (CO) staining) were obtained with
718 a ROM-380 freezing microtome. DAPI staining (2 μg/mL; Roche) was used to
719 determine L4 barrel field and to confirm whether IONs were cut properly. After DAPI
720 staining, slices were mounted with Anti-fade Mounting Medium (Longin et al., 1993),
721 and fluorescent images were acquired by a TCS SP5 confocal microscope. Cytochrome
722 oxidase (CO) staining was also used to confirm whether IONs were cut properly (data
723 not shown). Coronal sections were incubated with CO stain solution (0.05%
724 Cytochrome C (Sigma)/0.08% 3-3’ diaminobenzidine tetrahydrochloride (Nacalai
725 tesque)/30% sucrose in 0.1 M PB) for 4 h at 37°C. After visual detection of stain,
726 sections were washed 3 times with 0.1 M PB and mounted with EUKITT (Kindler).
727
728 Statistics and computing
729 Two-tailed parametric and nonparametric tests were used to show the differences among

means and medians, respectively (See Figure legends). The asterisks in the figures indicate the following: *$p < 0.05$, **$p < 0.01$, and ***$p < 0.001$. $p < 0.05$ was considered statistically significant. g and r indicate the effect size for parametric and for nonparametric tests, respectively (Field, 2009; Kline, 2004). Error bars in bar graphs and line graphs represent SEM. In box plots, upper and lower limits of box represent 75th and 25th percentile, crosses represent mean, horizontal lines represent median, upper and lower whiskers represent maximum and minimum within 1.5 interquartile range, and observations beyond the whisker range were marked with open circles as outliers. Brunner-Munzel test was performed by R 3.2.5 and its additional package lawstat 3.0. All other analyses and visualizations were performed using Fiji/ImageJ 1.51p (Schindelin et al., 2012) and custom-written scripts in Python 3.5.2 with its additional packages Numpy 1.11.3, Scipy 0.18.1, Matplotlib 1.5.1, Pandas 0.19.2, Lifelines 0.9.3.2, PIL 4.2.1, OpenCV 3.3.1, Scikit-learn 0.19.1, Glob 0.6.and their later versions.

Detailed information about samples used in each analysis was summarized in Table 1. Briefly, sample sizes were as follows.

Figure 2b: Group 1 (SS) (n = 35, 39, 38 and 33 neurons from 7, 8, 8 and 6 mice for P3, P4, P5, P6, respectively); Group 2 (SP) (n = 12, 12, 12 and 8 neurons from 5, 5, 5 and 3 mice for P3, P4, P5, P6, respectively). Figure 2e: Group 1 (SS) (n = 30, 38, 36 and 29 from 7, 8, 8 and 6 mice for P3, P4, P5, P6, respectively); Group 2 (SP) (n = 11, 12, 11 and 7 neurons from 5, 5, 5 and 3 mice for P3, P4, P5, P6, respectively).

Figures 3e and 3f: n = 28, 12, 36 and 18 BDs for $P3_L$ inside, $P3_L$ outside, $P6_L$ inside and $P6_L$ outside, respectively. Data were collected from 8 eSS neurons of 4 mice.

Figures 4d–4i: Data were collected from 8 eSS neurons of 4 mice. Four

neurons (n = 2 mice) were analyzed every 8 h between $P3_L$ and $P5_L$, and the other 4 neurons (n = 2 mice) were analyzed between $P4_E$ and $P5_L$ because at $P3_L$ cell morphology was not very clear due to clouding of the window. Figure 4i: Surviving inner BD trees (n = 9, 9, 7, 6, 4 and 1 trees for 1, 2, 3, 4, 5 and 6 surviving time-frames, respectively); Surviving outer BD trees (n = 3, 3, 3, 2 and 1 trees for 1, 2, 3, 4 and 5 surviving time-frames, respectively); Eliminated inner BD trees (n = 7, 2 and 1 trees for 1, 2 and 3 surviving time-frames, respectively); Eliminated outer BD trees (n = 19 and 1 trees for 1 and 2 surviving time-frames, respectively).

Supplementary Figures 3e and 3f: n = 15 eSS neurons from 7 mice, 15 cSS neurons from 5 mice and 7 iSS neurons from 2 mice at $P3_L$. n = 13 eSS neurons from 5 mice, 13 cSS neurons from 4 mice and 9 iSS neurons from 3 mice at $P6_L$. Supplementary Figure 3g: n = 8 eSS neurons from 4 mice, 7 cSS neurons from 2 mice and 7 iSS neurons from 2 mice at $P3_L$. n = 8 eSS neurons from 4 mice, 7 cSS neurons from 2 mice, 9 iSS neurons from 3 mice at $P6_L$.

Sample sizes were often different among time-points for following reasons. Some neurons at some time-points were excluded from the analyses because cranial windows were cloudy, and terminals of AD and/or BDs were not clearly visible. One neuron (neuron ID #231-9) was excluded from AD length analysis because its AD terminals were out of imaging range. Two neurons (neuron ID #313-1 and 2) were excluded from $P6_L$ analyses because the mouse died during the imaging session at $P5_L$ by an anesthesia problem. One neuron (neuron ID #314-1) was excluded from $P3_L$ analyses because the $P3_L$ imaging of the mouse was skipped.

REFERENCES

- Akhmetshina, D., Nasretdinov, A., Zakharov, A., Valeeva, G., and Khazipov, R. (2016). The Nature of the Sensory Input to the Neonatal Rat Barrel Cortex. J Neurosci *36*, 9922-9932.
- Ballester-Rosado, C.J., Albright, M.J., Wu, C.S., Liao, C.C., Zhu, J., Xu, J., Lee, L.J., and Lu, H.C. (2010). mGluR5 in cortical excitatory neurons exerts both cell-autonomous and -nonautonomous influences on cortical somatosensory circuit formation. J Neurosci *30*, 16896-16909.
- Callaway, E.M., and Borrell, V. (2011). Developmental sculpting of dendritic morphology of layer 4 neurons in visual cortex: influence of retinal input. J Neurosci *31*, 7456-7470.
- Carrillo, J., Nishiyama, N., and Nishiyama, H. (2013). Dendritic translocation establishes the winner in cerebellar climbing fiber synapse elimination. J Neurosci *33*, 7641-7653.
- Datwani, A., Iwasato, T., Itohara, S., and Erzurumlu, R.S. (2002). NMDA Receptor-Dependent Pattern Transfer from Afferents to Postsynaptic Cells and Dendritic Differentiation in the Barrel Cortex. Molecular and Cellular Neuroscience *21*, 477-492.
- Emoto, K. (2011). Dendrite remodeling in development and disease. Dev Growth Differ *53*, 277-286.
- Erzurumlu, R.S., and Gaspar, P. (2012). Development and critical period plasticity of the barrel cortex. Eur J Neurosci *35*, 1540-1553.
- Espinosa, J.S., Wheeler, D.G., Tsien, R.W., and Luo, L. (2009). Uncoupling dendrite growth and patterning: single-cell knockout analysis of NMDA receptor 2B. Neuron *62*, 205-217.
- Field, A. (2009). Discovering statistics using SPSS, third edition edn (New York: SAGE Publications).
- Fox, K. (2008). Barrel Cortex (Cambridge: Cambridge University Press).
- Fujishima, K., Horie, R., Mochizuki, A., and Kengaku, M. (2012). Principles of branch dynamics governing shape characteristics of cerebellar Purkinje cell dendrites. Development *139*, 3442-3455.
- Goodman, C.S., and Shatz, C.J. (1993). Developmental mechanisms that generate precise patterns of neuronal connectivity. Cell *72*, 77-98.
- Haas, K., Li, J., and Cline, H.T. (2006). AMPA receptors regulate experience-dependent dendritic arbor growth in vivo. Proc Natl Acad Sci U S A *103*, 12127-12131.

- Harris, R.M., and Woolsey, T.A. (1981). Dendritic plasticity in mouse barrel cortex following postnatal vibrissa follicle damage. J Comp Neurol *196*, 357-376.
- Holtmaat, A., Bonhoeffer, T., Chow, D.K., Chuckowree, J., De Paola, V., Hofer, S.B., Hubener, M., Keck, T., Knott, G., Lee, W.C.*, et al.* (2009). Long-term, high-resolution imaging in the mouse neocortex through a chronic cranial window. Nat Protoc *4*, 1128-1144.
- Holtmaat, A., and Svoboda, K. (2009). Experience-dependent structural synaptic plasticity in the mammalian brain. Nat Rev Neurosci *10*, 647-658.
- Inan, M., Lu, H.C., Albright, M.J., She, W.C., and Crair, M.C. (2006). Barrel map development relies on protein kinase A regulatory subunit II beta-mediated cAMP signaling. J Neurosci *26*, 4338-4349.
- Iwasato, T., Datwani, A., Wolf, A.M., Nishiyama, H., Taguchi, Y., Tonegawa, S., Knopfel, T., Erzurumlu, R.S., and Itohara, S. (2000). Cortex-restricted disruption of NMDAR1 impairs neuronal patterns in the barrel cortex. Nature *406*, 726-731.
- Iwasato, T., Erzurumlu, R.S., Huerta, P.T., Chen, D.F., Sasaoka, T., Ulupinar, E., and Tonegawa, S. (1997). NMDA receptor-dependent refinement of somatotopic maps. Neuron *19*, 1201-1210.
- Iwasato, T., Inan, M., Kanki, H., Erzurumlu, R.S., Itohara, S., and Crair, M.C. (2008). Cortical adenylyl cyclase 1 is required for thalamocortical synapse maturation and aspects of layer IV barrel development. J Neurosci *28*, 5931-5943.
- Katz, L.C., and Shatz, C.J. (1996). Synaptic activity and the construction of cortical circuits. Science *274*, 1133-1138.
- Kline, R. (2004). Beyond significance testing (Washington, DC: American Psychological Association).
- Kossel, A., Löwel, S., and Bolz, J. (1995). Relationships between dendritic fields and functional architecture in striate cortex of normal and visually deprived cats. The Journal of Neuroscience *15*, 3913-3926.
- Krugers, H.J., and Joels, M. (2014). Long-lasting Consequences of Early Life Stress on Brain Structure, Emotion and Cognition. In Behavioral Neurobiology of Stress-related Disorders, C.M. Pariante, and M.D. Lapiz-Bluhm, eds. (New York: Springer), pp. 81-92.
- Lübke, J., and Feldmeyer, D. (2007). Excitatory signal flow and connectivity in a cortical column: focus on barrel cortex. Brain Struct Funct *212*, 3-17.
- Lendvai, B., Stern, E.A., Chen, B., and Svoboda, K. (2000). Experience-dependent plasticity of dendritic spines in the developing rat barrel cortex in vivo. Nature *404*, 876-881.

- Li, H., Fertuzinhos, S., Mohns, E., Hnasko, T.S., Verhage, M., Edwards, R., Sestan, N., and Crair, M.C. (2013). Laminar and columnar development of barrel cortex relies on thalamocortical neurotransmission. Neuron *79*, 970-986.
- Lin, D.M., Wang, F., Lowe, G., Gold, G.H., Axel, R., Ngai, J., and Brunet, L. (2000). Formation of precise connections in the olfactory bulb occurs in the absence of odorant-evoked neuronal activity. Neuron *26*, 69-80.
- Lohmann, C., Finski, A., and Bonhoeffer, T. (2005). Local calcium transients regulate the spontaneous motility of dendritic filopodia. Nat Neurosci *8*, 305-312.
- Longin, A., Souchier, C., Ffrench, M., and Bryon, P.A. (1993). Comparison of anti-fading agents used in fluorescence microscopy: image analysis and laser confocal microscopy study. Journal of Histochemistry & Cytochemistry *41*, 1833-1840.
- Luo, W., Mizuno, H., Iwata, R., Nakazawa, S., Yasuda, K., Itohara, S., and Iwasato, T. (2016). Supernova: A Versatile Vector System for Single-Cell Labeling and Gene Function Studies in vivo. Sci Rep *6*, 35747.
- Matsui, A., Tran, M., Yoshida, A.C., Kikuchi, S.S., U, M., Ogawa, M., and Shimogori, T. (2013). BTBD3 controls dendrite orientation toward active axons in mammalian neocortex. Science *342*, 1114-1118.
- Mizuno, H., Hirano, T., and Tagawa, Y. (2007). Evidence for activity-dependent cortical wiring: formation of interhemispheric connections in neonatal mouse visual cortex requires projection neuron activity. J Neurosci *27*, 6760-6770.
- Mizuno, H., Ikezoe, K., Nakazawa, S., Sato, T., Kitamura, K., and Iwasato, T. (2018). Patchwork-Type Spontaneous Activity in Neonatal Barrel Cortex Layer 4 Transmitted via Thalamocortical Projections. Cell Rep *22*, 123-135.
- Mizuno, H., Luo, W., Tarusawa, E., Saito, Y.M., Sato, T., Yoshimura, Y., Itohara, S., and Iwasato, T. (2014). NMDAR-regulated dynamics of layer 4 neuronal dendrites during thalamocortical reorganization in neonates. Neuron *82*, 365-379.
- Narboux-Nême, N., Evrard, A., Ferezou, I., Erzurumlu, R.S., Kaeser, P.S., Laine, J., Rossier, J., Ropert, N., Sudhof, T.C., and Gaspar, P. (2012). Neurotransmitter release at the thalamocortical synapse instructs barrel formation but not axon patterning in the somatosensory cortex. J Neurosci *32*, 6183-6196.
- Niell, C.M., Meyer, M.P., and Smith, S.J. (2004). In vivo imaging of synapse formation on a growing dendritic arbor. Nat Neurosci *7*, 254-260.
- Portera-Cailliau, C., Pan, D.T., and Yuste, R. (2003). Activity-regulated dynamic behavior of early dendritic protrusions: evidence for different types of dendritic filopodia. J Neurosci *23*, 7129-7142.
- Portera-Cailliau, C., Weimer, R.M., De Paola, V., Caroni, P., and Svoboda, K.

(2005). Diverse modes of axon elaboration in the developing neocortex. PLoS Biol *3*, e272.

- Schindelin, J., Arganda-Carreras, I., Frise, E., Kaynig, V., Longair, M., Pietzsch, T., Preibisch, S., Rueden, C., Saalfeld, S., Schmid, B.*, et al.* (2012). Fiji: an open-source platform for biological-image analysis. Nat Methods *9*, 676-682.
- Sin, W.C., Haas, K., Ruthazer, E.S., and Cline, H.T. (2002). Dendrite growth increased by visual activity requires NMDA receptor and Rho GTPases. Nature *419*, 475-480.
- Staiger, J.F., Flagmeyer, I., Schubert, D., Zilles, K., Kotter, R., and Luhmann, H.J. (2004). Functional diversity of layer IV spiny neurons in rat somatosensory cortex: quantitative morphology of electrophysiologically characterized and biocytin labeled cells. Cereb Cortex *14*, 690-701.
- Sur, M., and Rubenstein, J.L. (2005). Patterning and plasticity of the cerebral cortex. Science *310*, 805-810.
- Takeo, Y.H., Kakegawa, W., Miura, E., and Yuzaki, M. (2015). RORalpha Regulates Multiple Aspects of Dendrite Development in Cerebellar Purkinje Cells In Vivo. J Neurosci *35*, 12518-12534.
- Waite, P.M.E., and Cragg, B.G. (1982). The Peripheral and Central Changes Resulting from Cutting or Crushing the Afferent Nerve Supply to the Whiskers. Proceedings of the Royal Society B: Biological Sciences *214*, 191-211.
- Wang, C.F., Hsing, H.W., Zhuang, Z.H., Wen, M.H., Chang, W.J., Briz, C.G., Nieto, M., Shyu, B.C., and Chou, S.J. (2017). Lhx2 Expression in Postmitotic Cortical Neurons Initiates Assembly of the Thalamocortical Somatosensory Circuit. Cell Rep *18*, 849-856.
- Wayman, G.A., Impey, S., Marks, D., Saneyoshi, T., Grant, W.F., Derkach, V., and Soderling, T.R. (2006). Activity-dependent dendritic arborization mediated by CaM-kinase I activation and enhanced CREB-dependent transcription of Wnt-2. Neuron *50*, 897-909.
- Whitford, K.L., Dijkhuizen, P., Polleux, F., and Ghosh, A. (2002). Molecular control of cortical dendrite development. Annu Rev Neurosci *25*, 127-149.
- Wong, R.O., and Ghosh, A. (2002). Activity-dependent regulation of dendritic growth and patterning. Nat Rev Neurosci *3*, 803-812.
- Woolsey, T.A., Dierker, M.L., and Wann, D.F. (1975). Mouse SmI cortex: qualitative and quantitative classification of golgi-impregnated barrel neurons. Proc Natl Acad Sci U S A *72*, 2165-2169.
- Woolsey, T.A., and Van der Loos, H. (1970). The structural organization of layer IV

in the somatosensory region (SI) of mouse cerebral cortex. The description of a cortical field composed of discrete cytoarchitectonic units. Brain Res *17*, 205-242.

- Wu, C.S., Ballester Rosado, C.J., and Lu, H.C. (2011). What can we get from 'barrels': the rodent barrel cortex as a model for studying the establishment of neural circuits. Eur J Neurosci *34*, 1663-1676.
- Yang, G., Pan, F., and Gan, W.B. (2009). Stably maintained dendritic spines are associated with lifelong memories. Nature *462*, 920-924.
- Zuo, Y., Lin, A., Chang, P., and Gan, W.B. (2005). Development of long-term dendritic spine stability in diverse regions of cerebral cortex. Neuron *46*, 181-189.

ACKNOWLEDGEMENT

First and foremost, I would like to express my sincere gratitude to my supervisor Dr. Takuji Iwasato for sharing his wisdom and guiding me with limitless kindness and patience. Without his invaluable support, I would not have been where I am today. I would also like to specially thank Dr. Hidenobu Mizuno with much appreciation. His stimulating suggestions and encouragement helped me to coordinate my path in science. He also gave me the technical advice and made important contributions to my project. I am forever indebted to them for all they have done for me. I extend my thanks to all my colleagues, Dr. Shota Katori, Dr. Ryohei Iwata, Dr. Ayumi Suzuki, Dr. Wenshu Luo, Mr. Ramasamy Kandasamy, Ms. Luwei Wang, Ms. Piu Banerjee, Ms. Minako Kanbayashi, Ms. Satoko Kouyama and Mr. Takuya Sato for making every day so much brighter and happier. Also, a heated discussion with them improved my project much sophisticated. I also appreciate my Progress Committee members, Dr. Akatsuki Kimura, Dr. Tatsumi Hirata, Dr. Koichi Kawakami and Dr. Hitoshi Sawa, and previous members, Dr. Yasushi Hiromi and Dr. Yumiko Saga for fruitful discussions. I have always been pleased with the assistance of all the staffs in NIG and SOKENDAI, especially NIG cafeteria Sweet Home, for their kind help, cooperation, and everyday delicious meals throughout my student life. Special thanks to JSPS research fellow for providing a scholarship, which gave me the time and energy to focus on the research. Finally, I owe a deep sense of gratitude to my loving family members. I am able to spend ordinary days in NIG only because of the support and kindness of them. I would like to return my gratitude and love to them.

952 **FIGURE LEGENDS**

953 **Figure 1. Long-term *in vivo* imaging of cortical L4 neurons in neonates.**

954 **(a)** (Left) A schematic of the barrel map in the mouse somatosensory cortex (barrel
955 cortex), which represents arrangement of whiskers on the face. (Right) The barrel map
956 is visualized by EGFP signals derived from the TCA-GFP Tg mouse. A confocal image
957 of tangential section (100 μm-thick) of barrel cortex L4 of P8 mouse is shown.
958 **(b)** Schematic drawing of the *in vivo* time-lapse imaging between P3 and P6. IUE: *in*
959 *utero* electroporation.
960 **(c)** The barrel map visualized in the whole brain of P8 TCA-GFP Tg mouse (Mizuno et
961 al., 2014).
962 **(d)** (Left) A 2-photon image of the barrel cortex L4 of $P6_L$ TCA-GFP mouse transfected
963 with Flpe-based Supernova RFP vector set (Luo et al., 2016) by *in utero* electroporation
964 at E14. TCA termini were visualized by EGFP (green) and a sparse population of L4
965 neurons were brightly labeled by RFP (magenta). (Right) Green signal was
966 computationally enhanced from the left panel to better show the barrel map.
967 **(e)** A very light (~20 mg) and small (7 × 2 × 0.5 mm) titanium bar was used.

968 **(f)** Representative image of pups (at P6) used for 3-d-long imaging [time-lapsed (TL)
969 pups] (arrows). During imaging intervals, TL pups received maternal care with other
970 littermates.
971 **(g)** Representative Z-stack images of Supernova-RFP-labeled L4 neurons (magenta)
972 and EGFP signals in TCA-GFP Tg mice. The same image as that of (d) is shown.
973 **(h)** Higher-magnification images of the neuron shown in (g) (square). A, anterior; M,
974 medial.
975 **(i)** Basal dendrites (BDs: black), apical dendrite (AD: red), and axon (blue) of the
976 neuron were traced and reconstructed in 3-dimensions. Barrel map (green) was
977 determined by EGFP signal.
978 **(j–l)** Another set of representative case corresponding to (g–i).
979 **(m)** Body weight change of TL (n = 6) and control (n = 29) pups [mean ± SEM (dense)
980 and individual (faint)]. $P3_L$-TL vs $P6_L$-TL: $p < 0.001$, $g = 4.369$, Paired t-test. $P6_L$-TL vs
981 $P6_L$-control: $p = 0.312$, $g = 0.348$, Welch's t-test.
982 **(n)** Barrel field areas were measured in tangential sections prepared from TL pups (n =
983 7) immediately after $P6_L$ imaging. As controls, normal pups at $P3_L$ (n = 5) and $P6_L$ (n =
984 5) were used. $P3_L$-control vs $P6_L$-control: $p < 0.001$, $g = 6.131$; $P3_L$-control vs $P6_L$-TL:

p = 0.001, g = 2.913; $P6_L$-control vs $P6_L$-TL: p = 0.995, g = 0.003; Welch's t-test with Holm's correction.

(o, q) Increase of total BD length (o) and tip number (q) of TL pup L4 neurons during 3-d-long imaging (n = 51 neurons from 8 mice). Mean ± SEM (dense) and values of individual neurons (faint) were shown.

(p, r) Total BD length (p) and tin number (r) of L4 neurons of TL (n = 36 neurons from 6 mice) and control (n = 9 neurons from 2 mice) pups at $P6_L$ (Length: p = 0.795, g = 0.078, Tip number: p = 0.288, g = 0.295, Welch's t-test). This analysis was done by *in vivo* imaging. For control pups, a cranial window/titanium bar was attached at $P6_L$.

Error bars: SEM. Scale bars: 500 μm (a), 2 mm (c), 150 μm (d, g, j) and 50 μm (h, k).

Figure 2. AD dynamics and morphological features of L4 neurons in early neonates

(a) Most L4 neurons possessed an AD at $P3_L$, while the majority of these neurons had shortened ADs by $P6_L$. The same neurons are colored the same. Arrows, AD tips; filled arrowheads, axons; open arrowheads, BD tips. M, medial; D, dorsal.

(b) Plots of the mean ± SEM (dense) and individual (faint) of AD length of Group 1 (red) and Group 2 (blue) neurons. See also Supplementary Figure 1.

(c, d) Examples of AD dynamics in Group 1 (c) and Group 2 (d) neurons. D, dorsal.

(e) The mean ± SEM (dense) and individual (faint) plots of total BD length of Group 1 (red) and Group 2 (blue) neurons.

Sample sizes for (b and e) are shown in the Methods.

(f) Representative BD traces of two Group 1 (SS) and two Group 2 (SP) neurons at $P3_L$. The boundaries of inside (barrel-center side) and outside (opposite side) were determined as described in Methods.

(g) The orientation bias index (OBI) of barrel-edge SS (eSS) neurons was significantly larger than that of barrel-edge SP (eSP) neurons at $P3_L$ ($p = 0.001$, $g = 2.135$, Welch's t-test: n = 15 eSS neurons from 7 mice and 7 eSP neurons from 4 mice).

(h) Even before the initiation of AD retraction, eSS neurons already exhibited a larger OBI than eSP neurons ($p = 0.007$, $g = 1.710$, Welch's t-test: n = 8 eSS neurons with intact AD from 6 mice and 7 eSP neurons from 4 mice).

(i) BD traces at $P6_L$ of the same neurons as Figure 2f. Green shades represent individual barrels (TCA clusters).

(j) The OBI of eSS neurons was significantly larger than that of eSP neurons at $P6_L$ ($p = 0.012$, $g = 2.604$, Welch's t-test: n = 13 eSS neurons from 5 mice and 4 eSP neurons from 2 mice).

Box plot interpretation is described in the Methods. Scale bars: 50 μm (a, c, d) and 25 μm (f).

Figure 3. eSS neurons increased BD orientation bias by inner BD tree-specific elaboration.

(a) (Top) Z-stack images of the same eSS neuron at $P3_L$ and $P6_L$. (Bottom) BDs are traced. Green shade represents the TCA cluster. Dashed lines represent the border of inside/outside. Black, BDs; Blue, axons. Scale bar: 50 μm.

(b) eSS neurons increased OBI of BD between $P3_L$ and $P6_L$ ($p = 0.028$, $g = 1.244$, $n = 8$ eSS neurons of 4 mice, Paired t-test).

(c) (Top) At $P3_L$, the number of inner BD trees was significantly larger than that of outer ones ($p < 0.001$, $r = 1.974$, Brunner-Munzel test). From $P3_L$ to $P6_L$, there were no significant increases in BD tree number both inside ($p = 0.160$, $r = 0.317$) and outside ($p = 0.137$, $r = 0.404$, Wilcoxon signed-rank test). $n = 8$ eSS neurons of 4 mice. (Bottom) Schematics showing origins of inner (orange dots) and outer (blue dots) BD trees. Dashed line: inside/outside border.

(d) The ratio of number of inner to total BD trees did not change between $P3_L$ and $P6_L$ ($p = 0.401$, $r = 0.198$, Wilcoxon signed-rank test. $n = 8$ eSS neurons of 4 mice).

(e) (Top) The length of individual BD trees was similar between inside and outside at $P3_L$ ($p = 0.809$, $g = 0.085$, Welch's t-test). The length of individual inner trees at $P6_L$ was significantly larger than that at $P3_L$ ($p < 0.001$, $g = 1.019$, Welch's t-test). On the other hand, there was no significant difference between the length of the individual outer trees at $P3_L$ and that at $P6_L$ ($p = 0.451$, $g = 0.401$, Welch's t-test). (Bottom) Schematics showing an inner tree (orange) and an outer tree (blue). Inner and outer trees are those whose origins are located inside and outside, respectively. Sample sizes are shown in Methods.

(f) (Top) The tip number of individual BD trees was similar between inner and outer trees at $P3_L$ ($p = 0.967$, $g = 0.013$, Welch's t-test). The tip number of individual inner trees at $P6_L$ was significantly larger than that at $P3_L$ ($p < 0.001$, $g = 0.939$, Welch's t-test). There was no significant difference between the tip number of individual outer trees at $P3_L$ and that at $P6_L$ ($p = 0.260$, $g = 0.498$, Welch's t-test). (Bottom) Orange dots represent tips of an individual inner tree, and blue dots represent tips of an individual outer tree.

p-values of (c–f) were corrected by Holm's correction. Box plot interpretation is described in Methods.

(g) eSS neurons establish BD orientation bias in neonatal stages through at least two distinct phases. During Phase I (approximately between P0 and P3), eSS neurons acquire the initial orientation bias, which is ascribed to the difference of BD tree number between inside and outside. In Phase II, starting approximately at P3, the number of BD trees is not much changed but BD orientation bias is reinforced by the differential elaboration of individual inner and outer BD trees.

Figure 4. BD tree dynamics of SS neurons with 8-hour intervals.

(a) (Top) Z-stack images of a representative eSS neuron from $P3_L$ to $P5_L$ with 8-hour interval. Gray asterisk, AD; green asterisk, axon. (Bottom) Traces of the neuron in upper panels. Arrows indicate newly formed inner (orange) and outer (blue) BD trees. Arrowheads indicate origin positions of eliminated inner (orange) and outer (blue) trees.

(b, c) Formation (b) and elimination (c) of BD trees were observed continuously from $P4_E$ to $P5_L$. Data were collected from the same 8 neurons (4 mice).

(d, e) Angles of origins of trees that were newly formed (d) and eliminated (e) between $P3_L$ and $P5_L$. Vertical line and center indicate inside/outside border and cell body position, respectively.

(f, g) Matrix of presence/absence of individual outer (f) and inner (g) trees. Each row represents an individual tree. Circles indicate time points at which the tree was present. Dots indicate time points at which the tree image was not acquired due to technical problems. Trees are sorted in order of the formation time and life span length.

(h) The surviving efficiency was significantly higher for inner trees than for outer trees ($p = 0.004$, $\chi^2 = 8.282$, Log-rank test). In these analyses, only BD trees that were newly formed during $P3_L$ to $P5_L$ are used. Shaded areas represent log-log transformed 95% confidence intervals. Sample sizes are shown in Table 2.

(i) Relationship between survival time-frames and mean length ± SEM of individual trees that were newly emerged during imaging sessions. “Surviving In” and “Surviving Out” indicate newly emerged inner and outer trees, respectively, that remained at $P5_L$. “Eliminated In” and “Eliminated Out” indicate newly emerged inner and outer trees, respectively, that disappeared by $P5_L$.

Sample sizes for (d−g and i) are shown in Methods.

(j) An example of outer tree that survived long and was elaborated over time (red). The same neuron as that of Figure 3a is shown. It should be noted that this outer tree extended its arbors toward the barrel side.

(k) An example of late born winner trees (red). The same neuron as that of Figure 4a is

shown. The winner tree that was first detected at $P4_L$.

Scale bars: 50 μm (a) and 25 μm (j, k).

Figure 5. BD tree dynamics in the absence of spatial bias of TCA inputs

(a, b) (Top) Z-stack images of a representative barrel-center SS (cSS) neuron (a) and ION-cut mouse SS (iSS) neuron (b). Gray asterisk, AD; green asterisk, axon. (Bottom) BD morphologies of the neuron shown in the upper panel. Arrows, newly formed BD trees; arrowheads, origin positions of eliminated trees. Scale bars: 50 μm.

(c, d) Histograms of length of individual BD trees of eSS (40 trees, 8 neurons, 4 mice; Mean ± SD = 64.98 ± 36.10 μm), cSS (35, 7, 2; 60.81 ± 36.35 μm) neurons and iSS (30, 7, 2; 62.92 ± 32.78 μm) neurons at $P3_L$ (c) and eSS (54 trees, 8 neurons, 4 mice; 145.37 ± 125.26 μm), cSS (43, 7, 2; 152.68 ± 92.53 μm) and iSS (47, 9, 3; 137.82 ± 78.24 μm) neurons at $P6_L$ (d). Orange: inner BD trees. Blue: outer BD trees. At $P3_L$ (eSS vs cSS: $p = 0.480$, $F = 1.014$; eSS vs iSS: $p = 0.595$, $F = 1.213$; cSS vs iSS: $p = 0.860$, $F = 1.230$, F-test with Holm's correction). At $P6_L$ (eSS vs cSS: $p = 0.044$, $F = 1.832$; eSS vs iSS: $p = 0.002$, $F = 2.563$; cSS vs iSS: $p = 0.134$, $F = 1.399$, F-test with Holm's correction). See also Supplementary Figures 3i and 3j.

(e, f) Matrix of presence/absence of individual trees of 7 cSS (2 mice) (e) and 9 iSS neurons (3 mice) (f).

(g) Number per cell of BD trees that were newly formed between $P4_E$ and $P5_L$ in eSS (8 neurons, 2 mice), cSS (7 neurons, 2 mice) and iSS neurons (9 neurons, 3 mice). eSS vs cSS: $p = 0.310$, $r = 0.403$; eSS vs iSS: $p = 0.008$, $r = 0.873$, cSS vs iSS: $p = 0.464$, $r = 0.188$, Brunner-Munzel test with Holm's correction.

(h) Number per cell of BD trees that were eliminated between $P3_L$ and $P5_L$ in eSS, cSS and iSS neurons. (eSS vs cSS: $p = 0.022$, $r = 0.793$; eSS vs iSS: $p < 0.001$, $r = 4.430$; cSS vs iSS: $p = 0.129$, $r = 0.417$, Brunner-Munzel test with Holm's correction). Box plot interpretation is described in the Methods.

Figure 6. Early ION cutting disrupts patterns of spontaneous activity.

(a) *In vivo* calcium imaging of the large-barrel field of the somatosensory cortex L4 of a normal TCA-GCaMP Tg mouse at P5, which expresses GCaMP6s in TCAs. TCA termini demonstrated "patchwork"-type spontaneous activity (Mizuno et al., 2018), in which each "activated zone" corresponds to a single barrel. Representative images of activated zones at 3 time-points and the merged image with pseudo color (top) and traces of boundaries for activated zones (bottom) are shown.

(b) A heat map of activated zone boundaries in all activated events observed in 15 minutes in the mouse.

(c) Positions of circular regions of interests (ROIs). In most cases, ROIs were numbered according to the principal component analysis (PCA) scores of the correlations of the fluorescence changes. In a few ROIs (ROIs 9−18), the original orders based on the PCA scores were manually rearranged to show B1, β and γ barrels clearly in correlation matrix (e). Color shades represent the positions of individual activated zones (i.e., barrels).

(d) (Left) Representative fluorescence signals taken from the ROIs. (Right) $\Delta F/F > 50\%$ were plotted to construct the raster plots. Orange vertical lines in the raster plots demonstrate synchronized activities among ROIs, which were confined to individual barrels.

(e) Correlation matrix constructed from the fluorescence changes of all ROI pairs.

(f) *In vivo* calcium imaging of the large-barrel field of the somatosensory cortex L4 of a TCA-GCaMP Tg mouse at P5, in which ION was cut at P0 (Early-ION-cut mouse). TCA termini demonstrated spontaneous activity that lacked the patchwork pattern. Individual activated zones are largely overlapped. Representative images of activated

zones at 3 time-points and the merged image with pseudo color (top) and traces of boundaries for activated zones (bottom) are shown.

(g) Heat maps of activated zone boundaries in all firing events observed in 15 minutes.

(h) Positions of ROIs in the Early-ION-cut mouse. All ROIs were numbered according to the PCA scores of the correlations of the fluorescence changes.

(i) Representative fluorescence signals and raster plots ($\Delta F/F > 50\%$) taken from the ROIs in the Early-ION-cut mouse. Orange vertical lines in the raster plots demonstrate synchronized activities among ROIs. Note that there were no specific clusters of ROIs.

(j) Correlation matrices constructed from the fluorescence changes of all ROI pairs in the Early-ION-cut mouse.

Scale bars: 150 μm.

(k) Sizes of individual activated zone of normal mice (336 zones in two P5 and one P6 mice) and ION-cut mice (304 zones in three P5 mice) are compared ($p < 0.001$, $g = 0.928$, Welch's t-test).

(l) The total counts of activated events in sequential 3 minutes in each ROI/each mouse. Orange circles: ROIs located on hollows, blue circles: ROIs on septa, gray circles: ROIs on ION-cut mice, black line: average of all ROIs of each mouse, red line: average of

ROIs on hollow of each mouse. Hollows and septa were determined manually. Data of (a–j) are from Mouse #1 and #5.

(m) Schematic depicting the experimental schedule.

Figure 7. Differential BD tree dynamics in neonatal barrel cortex SS neurons.

(a) In the normal neonatal mouse barrel cortex, eSS neurons receive spatially biased TCA inputs, predominantly from the barrel-center side (yellow); while on the other side (white), they receive no inputs or inputs from inappropriate TCAs. At P3, eSS neurons already have BD orientation bias, albeit weak, toward the barrel-center side (Figure 2g). However, at this age, individual BD trees are still primitive (Figures 2f, 3e and 3f) and the BD orientation bias is ascribed primarily to the larger number of BD trees on the barrel side versus the other side (Figure 3c). BD orientation bias increases drastically between P3 and P6 (Figure 3b), while the ratio of inner tree number to total tree number does not change (Figure 3d). BD trees are highly dynamic and emerge (orange) and disappear (dashed grey BDs) frequently both inside and outside the barrel center-side half (Figures 4a–e). Meanwhile, only a fraction of trees (mostly inner) are stabilized (Figures 4f–h) and these become extensively elaborated over time to become “winners”

(red) (Figure 4i). BD trees born later also have a chance to become winners (Figures 4j and 4k).

(b) cSS and iSS neurons receive TCA inputs (yellow) from all directions (no biased inputs). In this situation, BD tree turnover is suppressed (Figures 5g and 5h), few winners and losers are found, and most trees elaborate moderately (Figure 5d and Supplementary Figure 3j).

Supplementary Figure 1. Initiation timing and velocity of AD retraction vary among neurons even in the same animal.

(a) Plots of changes of AD length of Group 1 (SS) and Group 2 (SP) neurons between $P2_L$ and $P6_L$ (n = 8 mice). The mean ± SEM (dense) and individual (faint) values are shown. The data between $P3_L$ and $P6_L$ are the same as those of Fig. 2b.

(b–i) The plots of changes of AD length of individual neurons in each mouse. It is intriguingly that the initiation timing and velocity of AD retraction vary among neurons even in the same animals.

Supplementary Figure 2. Characteristics of BD trees of eSP neurons.

(a) The numbers of BD trees per cell. $P3_L$ inside vs $P3_L$ outside ($p = 0.856$, $r = 0.049$) and $P6_L$ inside vs $P6_L$ outside ($p = 0.809$, $r = 0.092$). n = 7, 7, 4, 4 neurons. Brunner-Munzel test.

(b) The lengths of individual BD trees. $P3_L$ inside vs $P3_L$ outside ($p = 0.641$, $g = 0.147$) and $P6_L$ inside vs $P6_L$ outside ($p = 0.617$, $g = 0.227$). n = 19, 21, 10, 11 trees. Welch's t-test.

(c) The tip numbers of individual BD trees. $P3_L$ inside vs $P3_L$ outside ($p = 0.572$, $g = 0.177$) and $P6_L$ inside vs $P6_L$ outside ($p = 0.846$, $g = 0.087$). n = 19, 21, 10, 11 trees. Welch's t-test.

Box plot interpretation is described in the Methods.

(d) Number per cell of BD trees that were newly formed between P4E and P5L in eSS (red: 8 neurons, 2 mice) and eSP (blue: 3 neurons, 1 mouse).

(e) Number per cell of BD trees that were eliminated between P4E and P5L in eSS (red: 8 neurons, 2 mice) and eSP (blue: 3 neurons, 1 mouse).

Supplementary Figure 3. Supplementary information for Figure 5.

(a) IONs were severed at P0 afternoon (Early-ION-cut mice).

(b) Confocal images of tangential slices after *in vivo* imaging at $P6_L$. Barrel maps

visualized by EGFP signals of TCA-GFP Tg mouse were impaired in Early-ION-cut mice. Scale bar: 400 μm.

(c) Early-ION-cut (75.3%: 55/73 neurons) and normal (67.8%: 40/59 neurons) mice had similar ratios of neurons without AD (red) at P16 ($p = 0.337$, $\chi^2 = 0.921$, χ^2 test).

(d) Schematic depicting the imaging schedule.

(e) Total BD length of eSS, cSS and iSS neurons at $P3_L$ (eSS vs cSS: $p = 0.894$, $g = 0.049$; eSS vs iSS: $p = 0.914$, $g = 0.291$; cSS vs iSS: $p = 1.071$, $g = 0.375$, Welch's t-test with Holm's correction) and $P6_L$ (eSS vs cSS: $p = 0.735$, $g = 0.135$; eSS vs iSS: $p < 0.001$, $g = 1.767$; cSS vs iSS: $p = 0.020$, $g = 1.100$, Welch's t-test with Holm's correction).

(f) Total BD tip number at $P3_L$ (eSS vs cSS: $p = 1.000$, $g = 0.000$; eSS vs iSS: $p = 1.004$, $g = 0.414$; cSS vs iSS: $p = 0.700$, $g = 0.389$, Welch's t-test with Holm's correction) and $P6_L$ (eSS vs cSS: $p = 0.305$, $g = 0.411$; eSS vs iSS: $p = 0.015$, $g = 1.249$; cSS vs iSS: $p = 0.185$, $g = 0.691$, Welch's t-test with Holm's correction).

(g) Number per cell of BD trees at $P3_L$ (eSS vs cSS: $p = 1.000$, $r = 0.000$; eSS vs iSS: $p = 0.761$, $r = 0.235$; cSS vs iSS: $p = 0.992$, $r = 0.271$, Brunner-Munzel test with Holm's correction) and $P6_L$ (eSS vs cSS: $p = 0.327$, $r = 0.263$; eSS vs iSS: $p = 0.248$, $r = 0.482$; cSS vs iSS: $p = 0.385$, $r = 0.343$, Brunner-Munzel test with Holm's correction).

(h) Length of individual BD trees of eSS, cSS and iSS neurons at $P3_L$, and $P6_L$. At $P3_L$: eSS vs cSS: p = 1.861, g = 0.115; eSS vs iSS: p =1.607, g = 0.059; cSS vs iSS: p = 0.807, g = 0.061, Welch's t-test with Holm's correction. At $P6_L$: eSS vs cSS: p = 0.742, g = 0.065; eSS vs iSS: p = 1.427, g = 0.071; cSS vs iSS: 1.246, g = 0.174, Welch's t-test with Holm's correction. See legends of Figures 5c and 5d for further information, including values of F-test.

(i, j) Cumulative curves of length of individual eSS-Inside, eSS-Outside, cSS and iSS BD trees at $P3_L$ (n = 28, 12, 35 and 30 trees) and $P6_L$ (n = 36, 18, 43 and 47 trees), respectively.

Sample sizes for (e–g) and box plot interpretation are shown in Methods. Error bars: SEM.

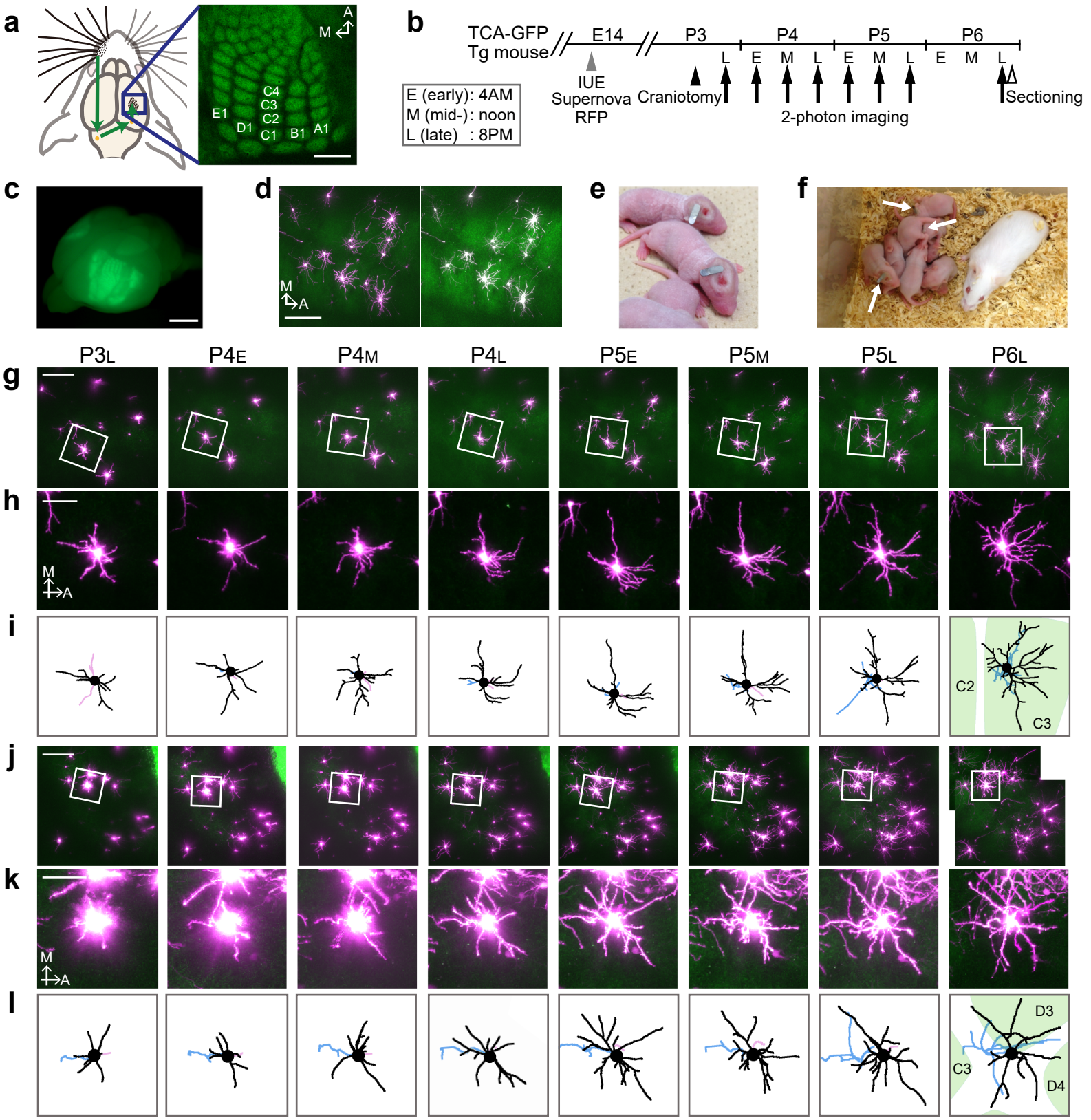
a
A
M
C4
C3
C2
C1
E1
D1
B1
A1
b
TCA-GFP
Tg mouse
E14
P3
P4
P5
P6
E (early): 4AM
M (mid-): noon
L (late) : 8PM
IUE
Supernova
RFP
Craniotomy
2-photon imaging
Sectioning
c
d
e
f
P3L
P4E
P4M
P4L
P5E
P5M
P5L
P6L
g
h
i
j
k
l
C2
C3
D3
D4
m
Body weight (g)
TL
Control
n
Barrel field size (mm²)
**
***
N.S.
o
Total BD length (μm)
p
Total BD length (μm)
N.S.
q
Total BD tip number
r
Total BD tip number
N.S.
Cont.
TL

Figure 1

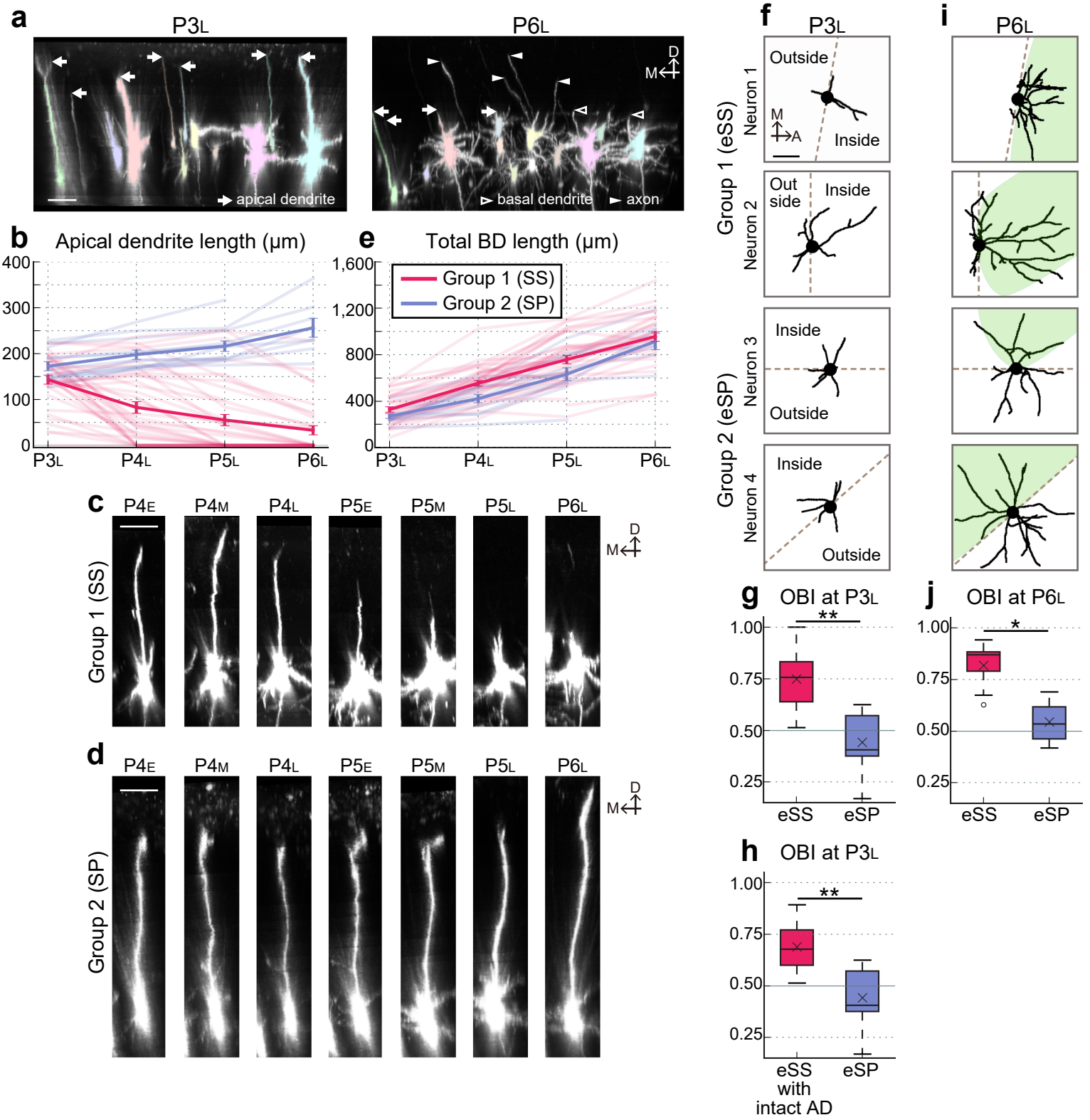
a
P3L
P6L
D
M
apical dendrite
basal dendrite
axon
b
Apical dendrite length (μm)
400
300
200
100
0
P3L
P4L
P5L
P6L
e
Total BD length (μm)
1,600
1,200
800
400
0
Group 1 (SS)
Group 2 (SP)
c
P4E
P4M
P4L
P5E
P5M
P5L
P6L
Group 1 (SS)
d
Group 2 (SP)
f
P3L
Outside
Inside
M
A
Out side
Group 1 (eSS)
Neuron 1
Neuron 2
Group 2 (eSP)
Neuron 3
Neuron 4
i
P6L
g
OBI at P3L
1.00
0.75
0.50
0.25
**
eSS
eSP
j
OBI at P6L
*
h
OBI at P3L
eSS with intact AD

Figure 2

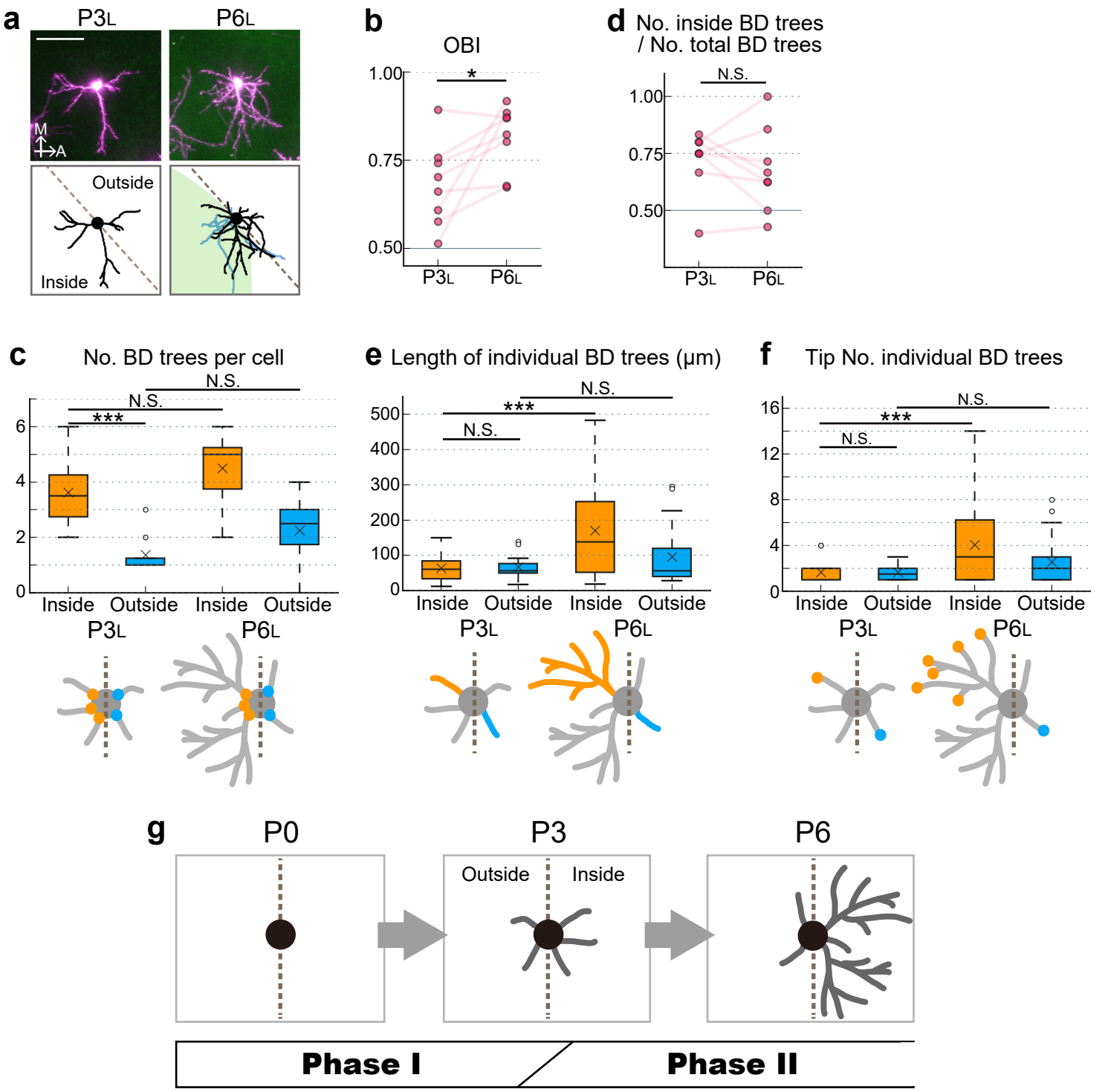
a
P3L
P6L
M
A
Outside
Inside
b
OBI
1.00
0.75
0.50
*
P3L
P6L
d
No. inside BD trees
/ No. total BD trees
N.S.
1.00
0.75
0.50
P3L
P6L
c
No. BD trees per cell
N.S.
N.S.
***
6
4
2
0
Inside
Outside
Inside
Outside
P3L
P6L
e
Length of individual BD trees (μm)
N.S.
***
N.S.
500
400
300
200
100
0
Inside
Outside
Inside
Outside
P3L
P6L
f
Tip No. individual BD trees
N.S.
***
N.S.
16
12
8
4
0
Inside
Outside
Inside
Outside
P3L
P6L
g
P0
P3
P6
Outside
Inside
Phase I
Phase II

Figure 3

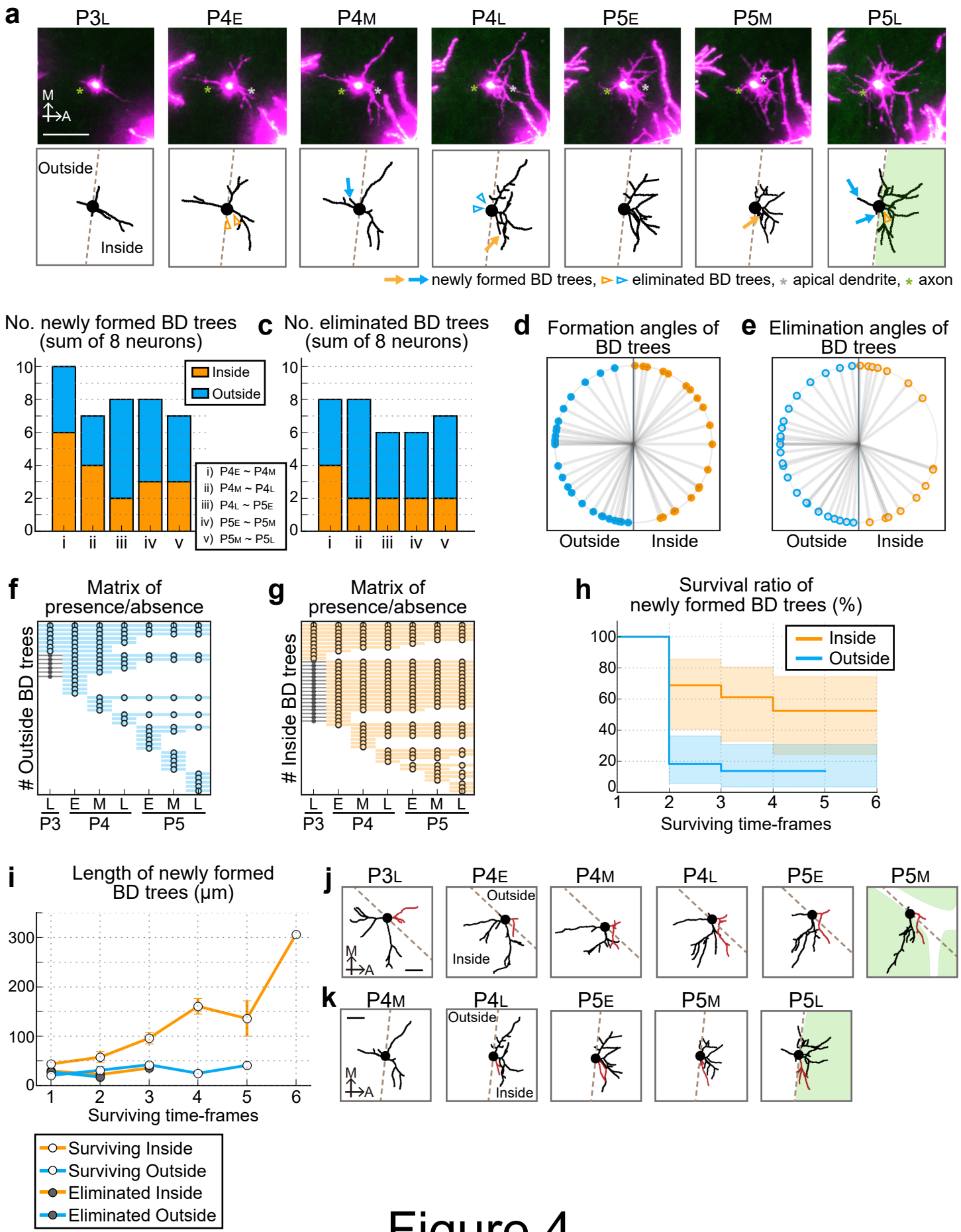
a
P3L
P4E
P4M
P4L
P5E
P5M
P5L
M
A
Outside
Inside
newly formed BD trees, eliminated BD trees, apical dendrite, axon
b
No. newly formed BD trees (sum of 8 neurons)
Inside
Outside
i) P4E ~ P4M
ii) P4M ~ P4L
iii) P4L ~ P5E
iv) P5E ~ P5M
v) P5M ~ P5L
c
No. eliminated BD trees (sum of 8 neurons)
d
Formation angles of BD trees
Outside
Inside
e
Elimination angles of BD trees
Outside
Inside
f
Matrix of presence/absence
Outside BD trees
L E M L E M L
P3 P4 P5
g
Matrix of presence/absence
Inside BD trees
L E M L E M L
P3 P4 P5
h
Survival ratio of newly formed BD trees (%)
Inside
Outside
Surviving time-frames
i
Length of newly formed BD trees (μm)
Surviving time-frames
Surviving Inside
Surviving Outside
Eliminated Inside
Eliminated Outside
j
P3L
P4E
Outside
Inside
P4M
P4L
P5E
P5M
k
P4M
P4L
Outside
Inside
P5E
P5M
P5L

Figure 4

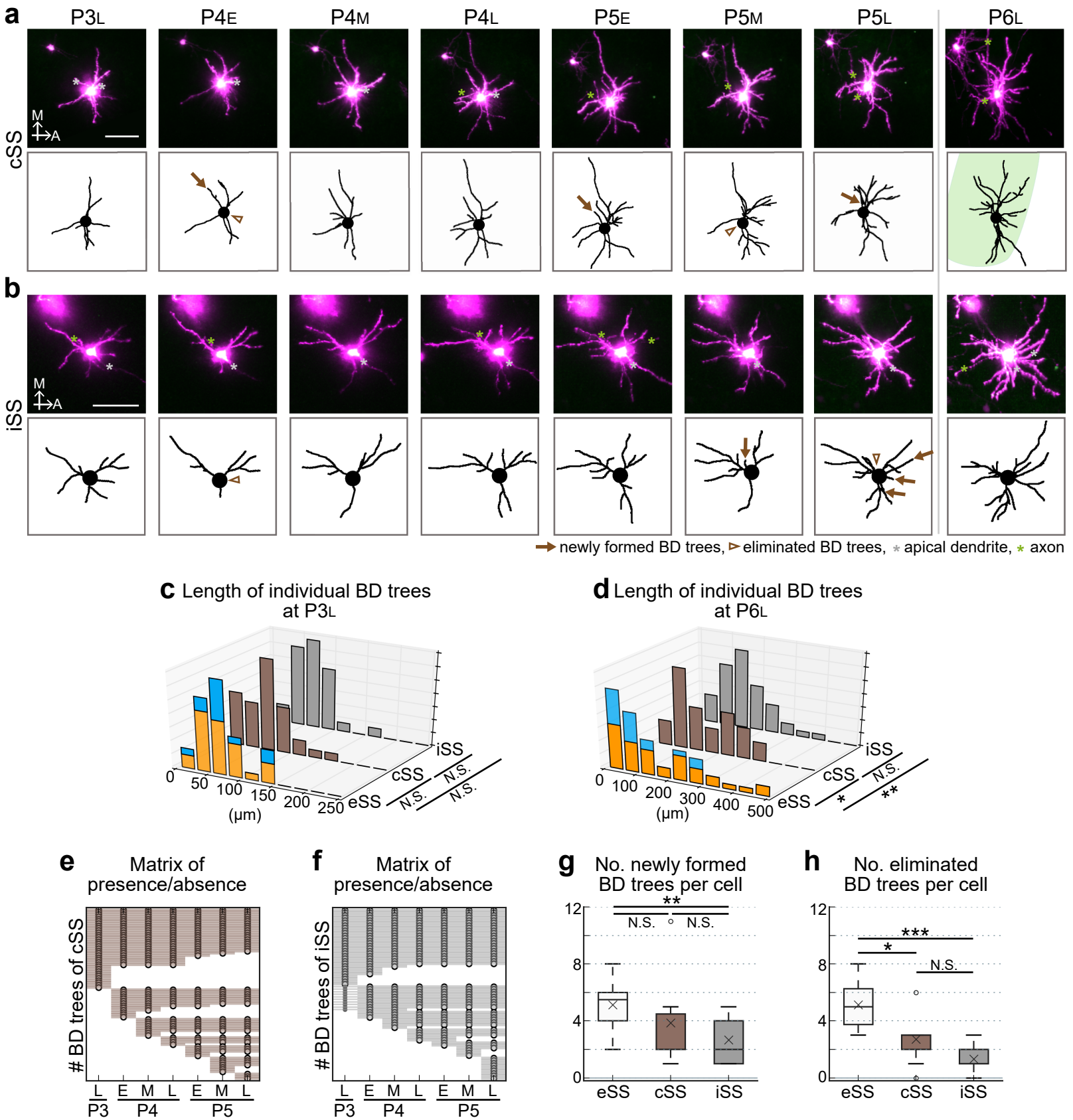
a
P3L
P4E
P4M
P4L
P5E
P5M
P5L
P6L
cSS
M
A
b
iSS
newly formed BD trees, eliminated BD trees, apical dendrite, axon
c Length of individual BD trees at P3L
0 50 100 150 200 250
(μm)
iSS
cSS
eSS
N.S.
N.S.
N.S.
d Length of individual BD trees at P6L
0 100 200 300 400 500
(μm)
iSS
cSS
eSS
N.S.
*
**
e Matrix of presence/absence
BD trees of cSS
L E M L E M L
P3 P4 P5
f Matrix of presence/absence
BD trees of iSS
L E M L E M L
P3 P4 P5
g No. newly formed BD trees per cell
**
N.S.
N.S.
12
8
4
0
eSS
cSS
iSS
h No. eliminated BD trees per cell
***
*
N.S.
12
8
4
0
eSS
cSS
iSS

Figure 5

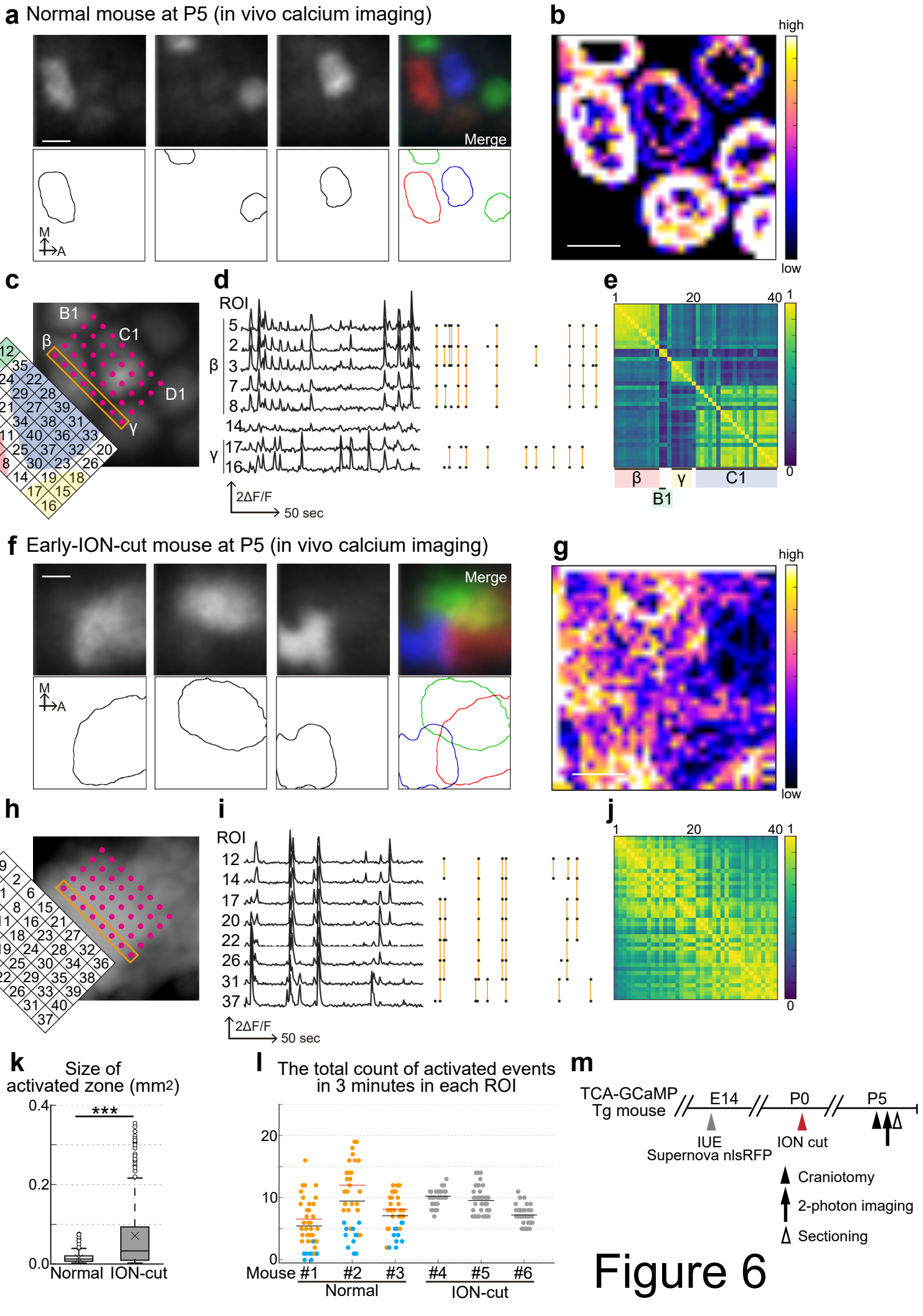
a Normal mouse at P5 (in vivo calcium imaging)
Merge
M
A
b
high
low
c
B1
C1
D1
β
γ
d
ROI
2ΔF/F
50 sec
e
1
20
40
β
γ
C1
B1
f Early-ION-cut mouse at P5 (in vivo calcium imaging)
g
h
i
j
k Size of activated zone (mm2)
***
Normal
ION-cut
l The total count of activated events in 3 minutes in each ROI
Mouse #1 #2 #3 #4 #5 #6
Normal
ION-cut
m
TCA-GCaMP Tg mouse
E14
P0
P5
IUE
Supernova nlsRFP
ION cut
Craniotomy
2-photon imaging
Sectioning

Figure 6

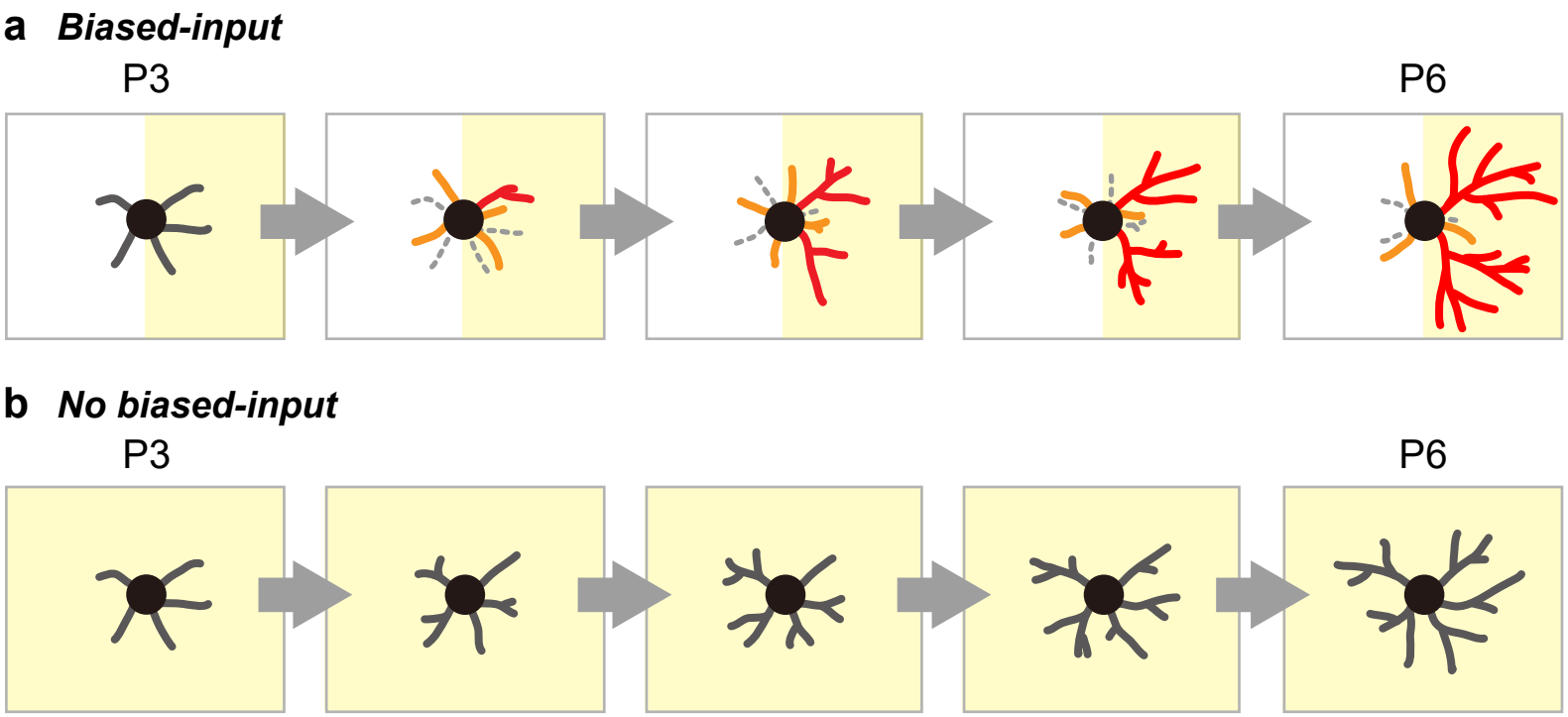

Figure 7

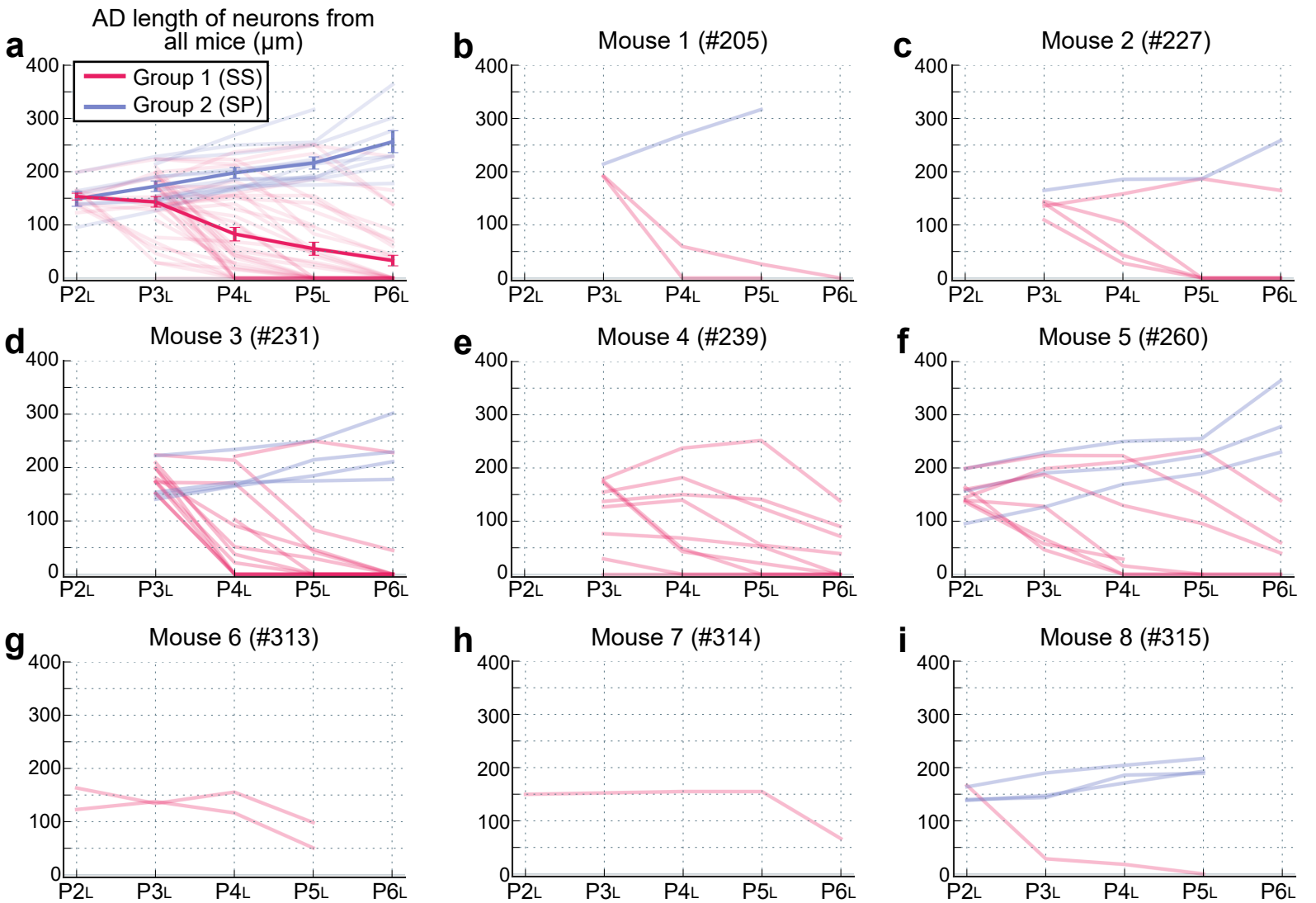

Supplementary Figure 1

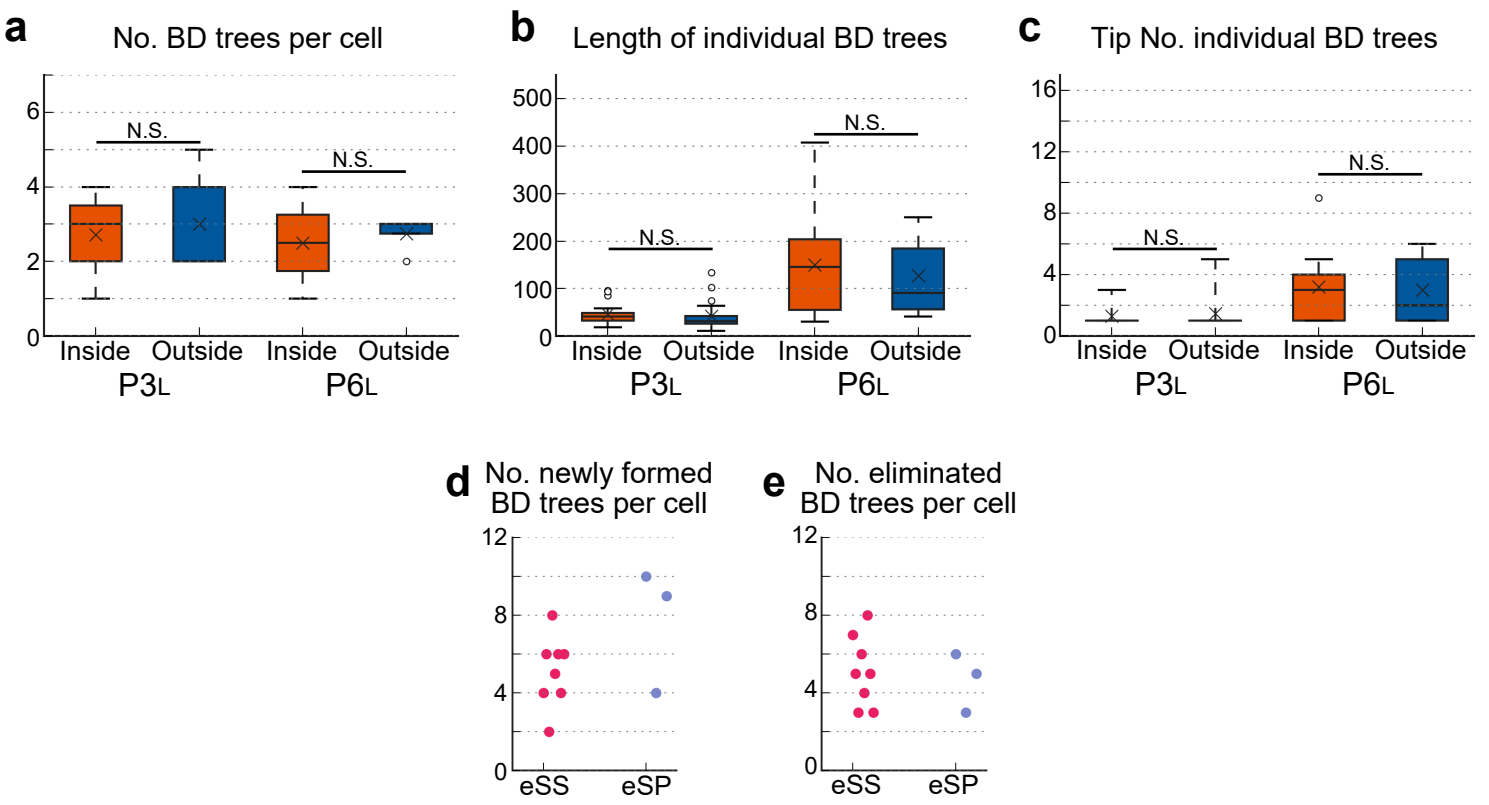

Supplementary Figure 2

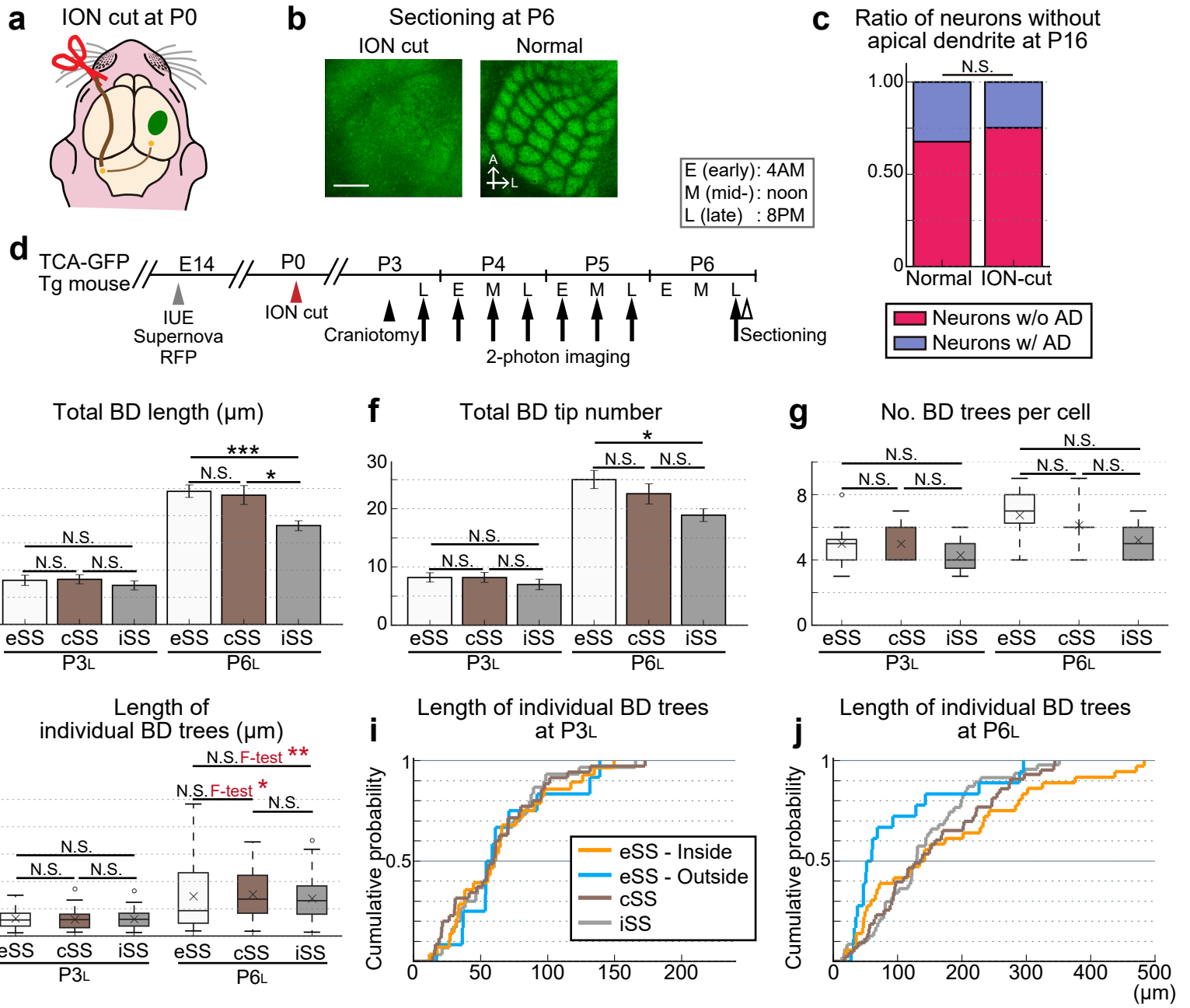

Supplementary Figure 3

Table 1. Summary of neurons which were used in each figure panel.

Neuron			Figure																		
ID (#)	Type[a]	Barrel[b]	2b				2e				2g[c]	2h[c],[d]	2j[c]	3b-f[c]	4b-i[c]	S2[c]		5c, d, S3g-j	5e-h	S3e, f	
			$P3_L$	$P4_L$	$P5_L$	$P6_L$	$P3_L$	$P4_L$	$P5_L$	$P6_L$						$P3_L$	$P6_L$			$P3_L$	$P6_L$
205-1	SS	C1	✓	✓	✓	✓	✓	✓	✓	✓	✓	✓	✓	✓				✓		✓	✓
205-3	SS	γ	✓	✓	✓	[g]	✓	✓	✓	[g]										✓	[g]
227-1	SS	C3	✓	✓	✓	✓	✓	✓	✓	✓	✓		✓	✓				✓		✓	✓
227-2	SS	B2	✓	✓	✓	✓	✓	✓	✓	✓	✓	✓	✓	✓				✓		✓	✓
227-3	SS	B1	✓	✓	✓	✓	✓	✓	✓	✓	✓	✓	✓	✓				✓		✓	✓
227-4	SS	C2	✓	✓	✓	✓	✓	✓	✓	✓										✓	✓
231-1	SS	D2	✓	✓	✓	✓	✓	✓	✓	✓	✓	✓	✓	✓	✓			✓	✓	✓	✓
231-2	SS	C2	✓	✓	✓	✓	✓	✓	✓	✓	✓	✓	✓	✓	✓			✓	✓	✓	✓
231-3	SS	C3	✓	✓	✓	✓	✓	✓	✓	✓								✓	✓	✓	✓
231-7	SS	D4	✓	✓	✓	✓	✓	✓	✓	✓								✓	✓	✓	✓
231-8	SS	C4	✓	✓	✓	✓	[g]	✓	✓	✓	[g]		✓		✓[j]				✓[j]	[g]	✓
231-9	SS	B4	[f]	✓	✓	✓	✓	✓	✓	✓										✓	✓
231-10	SS	D5	✓	✓	✓	✓	[g]	✓	✓	✓	[g]		✓		✓[j]				✓[j]	[g]	✓
231-11	SS	D6	✓	✓	✓	✓	[g]	✓	✓	✓	[g]	[g]	✓		✓[j]				✓[j]	[g]	✓
231-12	SS	D6	✓	✓	✓	✓	✓	✓	✓	✓										✓	✓
231-13	SS	D6	✓	✓	✓	✓	[g]	✓	✓	✓	[g]		✓		✓[j]				✓[j]	[g]	✓
231-15	SS	D5	[g]	✓	✓	✓	[g]	✓	✓	✓										[g]	✓
231-16	SS	E7	✓	✓	✓	✓	[g]	✓	✓	✓											
231-17	SS	D7	[g]	✓	✓	✓	[g]	✓	✓	✓											
239-1	SS	C2	✓	✓	✓	✓	✓	✓	✓	✓										✓	✓
239-2	SS	C2	✓	✓	✓	✓	✓	✓	✓	✓	✓		✓	✓	✓			✓	✓	✓	✓
239-3	SS	C3	✓	✓	✓	✓	✓	✓	✓	✓								✓	✓	✓	✓
239-4	SS	D3	✓	✓	✓	✓	✓	✓	✓	✓								✓	✓	✓	✓
239-6	SS	C4	✓	✓	✓	✓	✓	✓	✓	✓	✓	✓	✓	✓	✓			✓	✓	✓	✓
239-7	SS	C4	✓	✓	✓	✓	✓	✓	✓	✓								✓	✓	✓	✓
239-8	SS	D3	✓	✓	✓	✓	[g]	[g]	✓	✓											
239-9	SS	D4	✓	✓	✓	✓	✓	✓	✓	✓								✓	✓	✓	✓
239-10	SS	D4	✓	✓	✓	✓	✓	✓	✓	✓								✓	✓	✓	✓
260-1	SS	B4	✓	✓	✓	✓	✓	✓	✓	✓										✓	✓
260-3	SS	B4	✓	✓	✓	✓	✓	✓	[g]	[g]	✓		[g]							✓	[g]
260-5	SS	C3	✓	✓	[g]	[g]	✓	✓	[g]	[g]	✓		[g]							✓	[g]
260-6	SS	C4	✓	✓	✓	✓	✓	✓	✓	[g]										✓	[g]
260-7	SS	B3	✓	✓	✓	✓	✓	✓	✓	[g]	✓	✓	[g]							✓	[g]
260-9	SS	B2	✓	✓	✓	✓	✓	✓	[g]	[g]										✓	[g]
260-10	SS	B3	✓	✓	✓	[g]	✓	✓	✓	[g]	✓		[g]							✓	[g]
313-1	SS	C3	✓	✓	✓	[h]	✓	✓	✓	[h]	✓	✓	[h]							✓	[h]

313-2	SS	B2	✓	✓	✓	h)	✓	✓	✓	h)	✓		h)							✓	h)
314-1	SS	C2	i)	✓	✓	✓	i)	✓	✓	✓	i)	i)	✓							i)	✓
315-2	SS	C4	✓	✓	✓	g)	✓	✓	✓	g)	✓		g)							✓	g)
205-2	SP	γ	✓	✓	✓	g)	✓	✓	✓	g)											
227-5	SP	C4	✓	✓	✓	✓	✓	✓	✓	✓	✓	✓	✓			✓	✓				
231-4	SP	D3	✓	✓	✓	✓	✓	✓	✓	✓											
231-5	SP	D3	✓	✓	✓	✓	✓	✓	✓	✓	✓	✓	✓			✓	✓				
231-6	SP	D3	✓	✓	✓	✓	✓	✓	✓	✓	✓	✓	✓			✓	✓				
231-14	SP	D5	✓	✓	✓	✓	g)	✓	✓	✓	g)	g)	✓			g)	✓				
260-2	SP	B4	✓	✓	✓	✓	✓	✓	✓	✓											
260-8	SP	B3	✓	✓	✓	✓	✓	✓	g)	g)	✓	✓	g)			✓	g)				
260-11	SP	C4	✓	✓	✓	✓	✓	✓	✓	✓											
315-1	SP	C4	✓	✓	✓	g)	✓	✓	✓	g)	✓	✓	g)			✓	g)				
315-3	SP	C3	✓	✓	✓	g)	✓	✓	✓	g)	✓	✓	g)			✓	g)				
315-4	SP	C3	✓	✓	✓	g)	✓	✓	✓	g)	✓	✓	g)			✓	g)				
269-2 e)	SS	N/A																✓ j)	✓ j)	g)	✓
269-5 e)	SS	N/A																✓ j)	✓ j)	g)	✓
270-1 e)	SS	N/A																✓	✓	✓	✓
270-2 e)	SS	N/A																✓	✓	✓	✓
270-3 e)	SS	N/A																✓	✓	✓	✓
270-4 e)	SS	N/A																✓	✓	✓	✓
270-6 e)	SS	N/A																✓	✓	✓	✓
356-1 e)	SS	N/A																✓	✓	✓	✓
356-3 e)	SS	N/A																✓	✓	✓	✓

Note:

a) SS: spiny stellate neuron, SP: star pyramid neuron.

b) Barrel column to which the neuron belongs.

c) Neurons located at barrel edge were used (eSS and eSP).

d) eSS with intact AD and eSP were used.

e) ION cut mice.

f) Unanalyzable because AD terminal was out of imaging range.

g) Unanalyzable due to clouded window.

h) Unanalyzable due to death of pup.

i) Imaging was skipped.

j) $P3_L$ was not analyzed due to clouded window.

Table 2. Survival-table of newly formed BDs in Figure 4h.

Surviving time-frame	Eliminated outer BDs	n of surviving outer BDs	Eliminated inner BDs	n of survived inner BDs
1	-	22	-	16
2	18	4	5	9
3	1	2	1	7
4	0	1	1	4
5	0	0	0	1
6	-	-	0	1